

## Environmental Controls on the Simulated Diurnal Cycle of Warm-Season Precipitation in the Continental United States

S. B. TRIER, C. A. DAVIS, AND D. A. AHJEVYCH

*National Center for Atmospheric Research,\* Boulder, Colorado*

(Manuscript received 1 July 2009, in final form 30 September 2009)

### ABSTRACT

The diurnal cycle of warm-season precipitation in the Rocky Mountains and adjacent Great Plains of the United States is examined using a numerical modeling framework designed to isolate the role of terrain-influenced diurnally varying flows within a quasi-stationary longwave pattern common to active periods of midsummer convection. Simulations are initialized using monthly averaged conditions and contain lateral boundary conditions that vary only with the diurnal cycle. Together these attributes mitigate effects of transient weather disturbances originating upstream of the model domain. After a spinup period, the final 7 days of the 10-day model integration are analyzed and compared with observations. Results indicate that many salient features of the monthly precipitation climatology are reproduced by the model. These include a stationary afternoon precipitation frequency maximum over the Rocky Mountains followed overnight by an eastward-progressing zone of maximum precipitation frequencies confined to a narrow latitudinal corridor in the Great Plains. The similarity to observations despite the monthly averaged initial and lateral boundary conditions suggests that although progressive weather disturbances (e.g., mobile cold fronts and midtropospheric short waves) that originate outside of the region may help enhance and focus precipitation in individual cases, they are not crucial to the general location and diurnal cycle of midsummer precipitation. The roles of persistent daily features such as the nocturnal low-level jet and the thermally induced mountain-plains vertical circulation on both convection and a mesoscale water budget of the central Great Plains (where the heaviest rain occurs) are discussed.

### 1. Introduction

#### *a. Background*

An interesting aspect of the diurnal cycle of warm-season precipitation in the lee of major mountain ranges is its substantially delayed onset over the adjacent plains with respect to the solar heating cycle (e.g., Wallace 1975). Recent studies (Carbone et al. 2002; Carbone and Tuttle 2008) have established climatological phase coherence between afternoon convection at the foot of the Rocky Mountains and later convection on the Great Plains of the United States. Similar properties of the diurnal cycle of precipitation have been established in

the lee of major topography on other continents including East Asia (Wang et al. 2004), tropical northern Africa (Laing et al. 2008), and South America (A. J. Pereira Filho et al. 2009, unpublished manuscript), suggesting a fundamental linkage between afternoon mountain convection and subsequent propagating nocturnal convection.

Tripoli and Cotton (1989a,b) were among the first to simulate the diurnal cycle over the mountains and the adjacent plains using a model that permitted explicit deep convection. Based on their two-dimensional simulations, they explained the life cycle of warm-season convection in the lee of the mountains and adjacent plains as an outgrowth of the thermally forced west-to-east mountain-plains solenoid (MPS) modified by latent heat release from deep convection. However, earlier case studies (e.g., Wetzell et al. 1983) and recent observationally based climatologies (e.g., Tuttle and Davis 2006) indicate that warm-season nocturnal convection is often confined to narrow ( $<5^\circ$ ) latitudinal corridors and is strongly influenced by meridionally varying features

---

\* The National Center for Atmospheric Research is sponsored by the National Science Foundation.

---

*Corresponding author address:* Stanley B. Trier, National Center for Atmospheric Research, P.O. Box 3000, Boulder, CO 80307-3000.  
E-mail: trier@ucar.edu

such as quasi-stationary surface fronts and the nocturnal low-level jet (LLJ). Tuttle and Davis found that corridor events, consisting of a series of mesoscale convective systems (MCSs), typically persist for 2–7 days, and sometimes for more than 10. This longevity underscores their importance to the regional hydrologic cycle emphasized earlier by Fritsch et al. (1986).

Trier et al. (2006) used three-dimensional explicit simulations to diagnose factors influencing the behavior of nocturnal convection during a 7-day corridor event. They similarly concluded that meridionally varying features were important in focusing the nocturnal convection, whose overall eastward progression during its most intense stage was reasonably well explained by the vertically integrated buoyancy associated with the convection. Their corridor possessed a large fraction of long-lived ( $T > 12$  h) continuous rain events tied to precursor mid-tropospheric perturbations originating from west of the mountains and featured midtropospheric westerly flow of  $15\text{--}20\text{ m s}^{-1}$  with strong vertical shear in the layer below.

### b. Objectives

The goal of the current study is to discern the basic role of terrain-induced wind systems (e.g., MPS, LLJ) on the diurnal cycle of summertime convective precipitation under control of a common quasi-stationary midsummer large-scale pattern. This large-scale pattern (section 2) also supports west–east-oriented corridors of convection but has weaker midtropospheric flow than the environment that supported convection in Trier et al. (2006).

An interesting aspect of the nocturnal convection east of the mountains is that it *propagates* in the sense that its overall motion is not consistent with a layer-average environmental flow (Carbone et al. 2002). Here, propagation is not surprising given that the constituent MCSs of these rainfall episodes are large precipitation systems that may generate a host of organizing unbalanced internal circulations such as gravity waves, density currents, and bores (e.g., Carbone et al. 1990). Large, long-lived MCSs can also generate balanced internal circulations associated with a distinct mesoscale potential vorticity (PV) distribution that can help sustain them and influence their propagation (e.g., Tripoli and Cotton 1989b; Raymond and Jiang 1990; Olsson and Cotton 1997). However, it is also well known that environmental features can significantly influence aspects of the convection, including its propagation. For example, LLJ intensity and orientation (e.g., Corfidi et al. 1996), as well as warm advection (Jirak and Cotton 2007) associated with the LLJ, have been employed in empirically based MCS motion prediction methods.

Herein, we examine environmental factors governing the propagating nocturnal phase of convection following

nearly stationary daytime mountain convection. In addition to focusing on mechanisms supporting nocturnal convection on the plains, we also examine factors suppressing daytime convection in this location ( $\sim 100^{\circ}\text{--}95^{\circ}\text{W}$ ).

### c. Approach

A three-dimensional mesoscale atmospheric model with explicit convection (section 3) is used to simulate the midsummer diurnal precipitation cycle for 10 days. A high-resolution grid with explicit convection is deemed necessary since studies using coarser climate models have had difficulty in accurately representing both the timing of the onset of convection and its subsequent propagation (Dai et al. 1999; Lee et al. 2007). Simulations using numerical weather prediction models with mesoscale resolutions have had somewhat better success (e.g., Zhang et al. 2003). However, even these models are exposed to errors associated with required cumulus parameterizations, which contribute to propagation error by improperly representing the internal dynamics of the convection (Davis et al. 2003; Moncrieff and Liu 2006).

We use a monthly averaged initial condition representative of the midsummer flow and thermodynamic regimes (section 2) along with lateral boundary conditions constructed from the monthly average for which the only temporal variations are diurnal. Here, the averaging in the initial and lateral boundary conditions mitigates effects of external transient disturbances (e.g., midtropospheric short waves) on the model solution. This allows us to more easily isolate and explain how diurnally varying terrain-induced flows impact the diurnal cycle of precipitation. The characteristics of the simulated precipitation are compared to the observed monthly characteristics in section 4. The role of the MPS on the diurnal precipitation cycle is discussed in section 5 and the roles of additional environmental mechanisms such as quasi-stationary surface fronts and the LLJ in influencing nocturnal precipitation corridors are examined in section 6. The characteristic of precipitation corridors having heavy rainfall over approximately the same area on repeated nights raises questions concerning the roles of local versus remote moisture sources (e.g., Trenberth 1999) on the water cycle of the central Great Plains (CPL). We present a mesoscale water budget that addresses such questions in section 7.

## 2. Overview of precipitation and large-scale conditions for July 2001

### a. Precipitation

July 2001 was an active month across the mountains and adjacent plains of United States with eastward-progressing

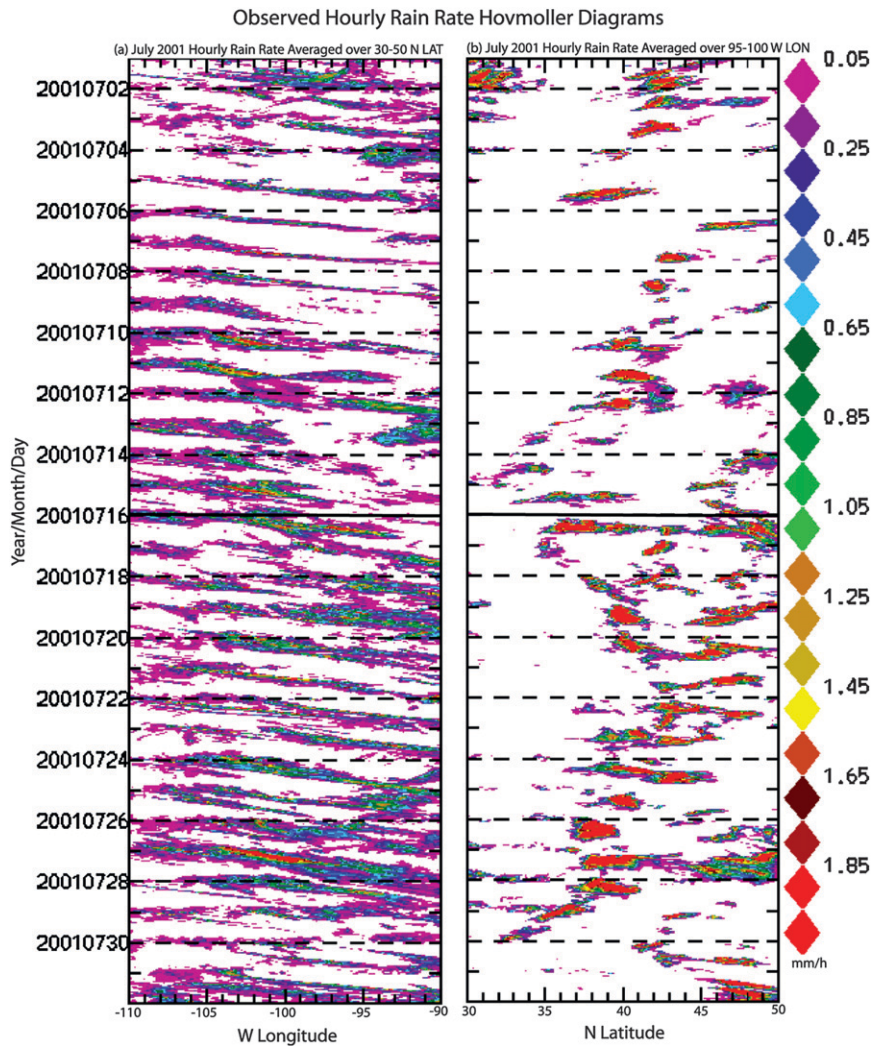


FIG. 1. Radar-derived rain-rate ( $\text{mm h}^{-1}$ ) Hovmöller diagrams for July 2001: (a) time-longitude diagram averaged from  $30^{\circ}$  to  $50^{\circ}\text{N}$  and (b) time-latitude diagram averaged from  $95^{\circ}$  to  $100^{\circ}\text{W}$ .

rain streaks (e.g., Carbone et al. 2002) occurring almost daily (Fig. 1a). The time-longitude and time-latitude rain-rate diagrams in Fig. 1 were derived from Weather Surveillance Radar-1988 Doppler (WSR-88D) at 2-km horizontal resolution using the methodology and WSI Corporation National Operational Weather Radar (NOWrad) dataset employed in Carbone et al. (2002). A time-longitude precipitation frequency diagram (Fig. 2a) exhibits a strong relationship to the diurnal cycle, with a stationary afternoon mountain rainfall frequency maximum and an eastward-progressing nocturnal maximum on the plains.

Also evident are multiple preferred latitudinal corridors of large rainfall frequency (Fig. 1b). There is some meandering of these corridors over time scales of a few days to weeks (Fig. 1b), but there are clearly preferred

latitudinal regions of large rainfall frequency over the CPL (Fig. 2b) with almost exclusively nocturnal precipitation.

#### b. Large-scale conditions

July 2001 exhibited a common midsummer 500-hPa pattern with an anticyclone over the southern Great Plains/Rockies and a trough over the western United States (Fig. 3a). The southerly flow brings moist mid-level conditions into the southern and central Rockies promoting regular afternoon convection (sections 5 and 6). This large-scale condition also supports latitudinal corridors of convection that extend eastward onto the plains, as Tuttle and Davis (2006) found a similar location of the upper-level anticyclone during multiday corridor events.

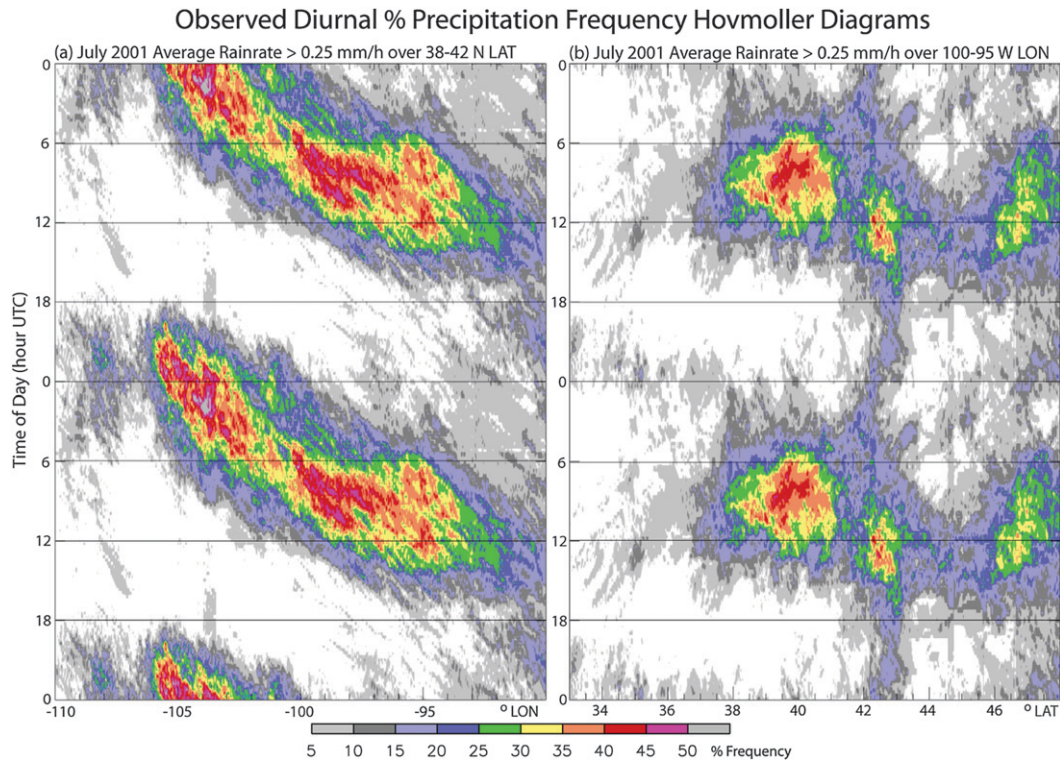


FIG. 2. Diurnal frequency diagrams of rain rate exceeding  $0.25 \text{ mm h}^{-1}$  for July 2001 for the regions averaged (a) from  $38^\circ$  to  $42^\circ\text{N}$  and (b) from  $95^\circ$  to  $100^\circ\text{W}$ .

The northernmost corridor of large precipitation frequency (Fig. 2b) is likely influenced by baroclinic disturbances. In contrast, the southernmost corridor near  $40^\circ\text{N}$  (Fig. 2b) occurs within weak midlevel flow (Fig. 3a) but has relatively large convective available potential energy (CAPE) (Fig. 3b). Although weaker than what is typically found in individual latitudinal corridors of convection (e.g., Trier et al. 2006; Tuttle and Davis 2006), a west–east-oriented surface baroclinic zone is clearly evident over the CPL in the monthly averaged condition (Fig. 3b).

### 3. Numerical model, experiment design, and analysis

Our goal is to simulate a generic diurnal cycle of warm season precipitation rather than one specifically representative of July 2001. We choose July 2001 on which to base our simulations because of its greater than normal frequency of coherent long-lived eastward-progressing rain streaks. Here we assume that the monthly averaging used to formulate initial and lateral boundary conditions weakens the forcing for deep convection but preserves the overall character of the relatively common midsummer long-wave pattern in which convection develops.

#### a. Modeling system

We integrate the Advanced Research Weather Research and Forecasting (WRF) model, version 3 (Skamarock et al. 2005) for 10 days over the single subcontinental domain depicted in Fig. 4a. In these integrations WRF is coupled with the Noah land surface model (Ek et al. 2003). The basic principles underlying the coupling are provided in Chen and Dudhia (2001). The model contains  $900 \times 600$  horizontal grid points with 3-km horizontal spacing. While this spacing does not provide resolution sufficient to fully resolve individual convective cells (Bryan et al. 2003), it affords adequate representation of mesoscale properties of convective systems and thus obviates the need for cumulus parameterization. The vertical grid contains 44 levels and is stretched to allow spacing of less than 100 m near the lowest model grid point to  $\sim 700$  m near the model top near 21 km. The model is initialized using average 0000 UTC Eta Model analysis conditions for July 2001 (Fig. 3) with lateral boundary conditions derived from the monthly average that vary at 3-h intervals.

The PBL scheme used in the simulations (Janjić 1990, 1994) predicts turbulent kinetic energy and allows vertical mixing between individual model layers. Other physical parameterizations include a bulk microphysics

### Average 00 UTC Eta Model Analyses for July 2001

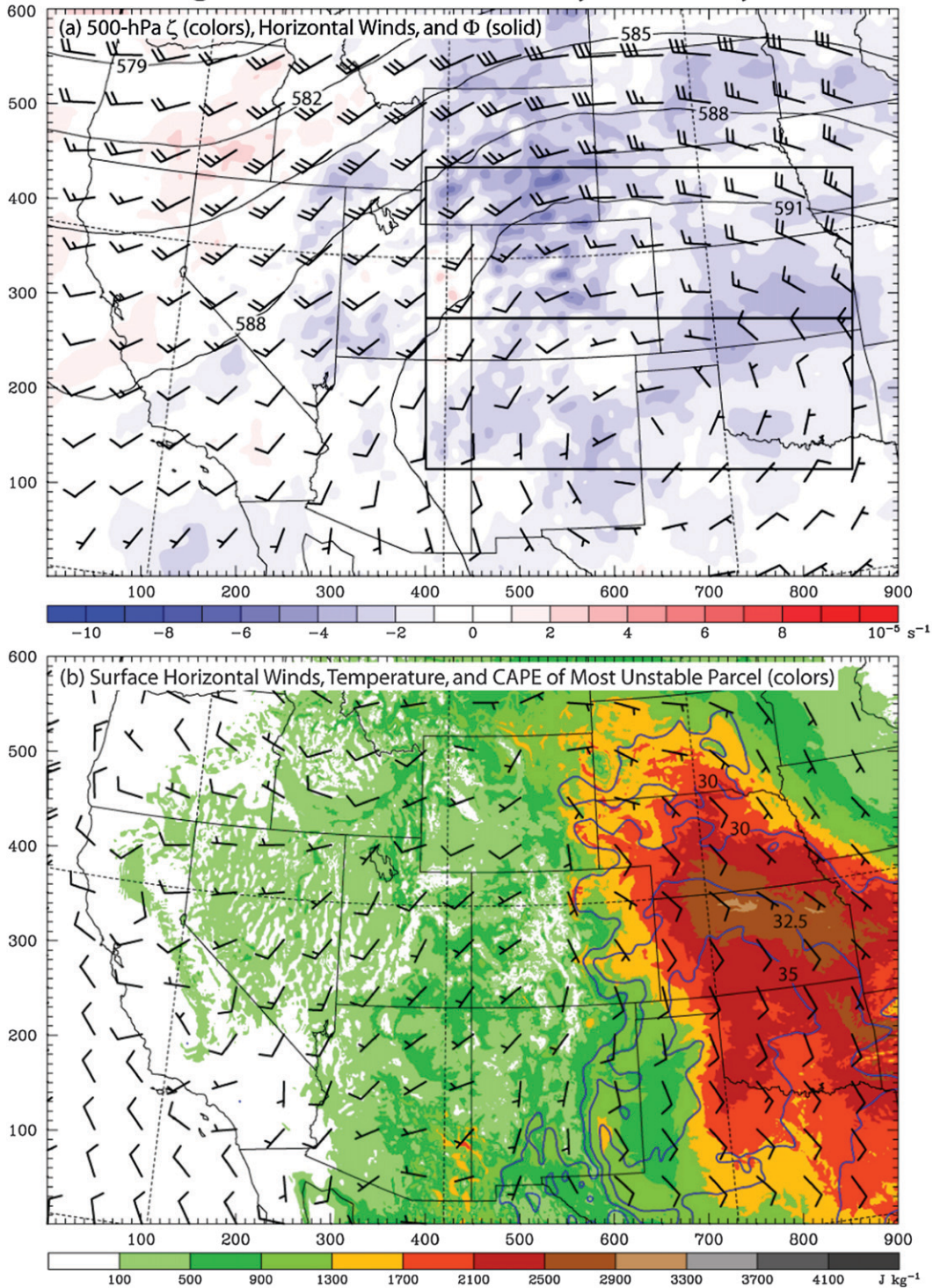


FIG. 3. Monthly averaged 0000 UTC fields for July 2001 derived from Eta Model gridded analyses. (a) 500-hPa relative vorticity (colors), horizontal wind, and geopotential height (3-dam solid contour intervals). The rectangles indicate the location of the  $y$ -averaged  $x$ - $z$  cross sections presented in Fig. 9. (b) Surface horizontal wind and CAPE (colors) for 500-m deep air parcels containing the maximum equivalent potential temperature in a vertical column, along with surface temperature, are analyzed east of the continental divide ( $\sim 105^\circ\text{W}$ ) with a  $2.5^\circ\text{C}$  contour interval ranging from  $30^\circ$  to  $35^\circ\text{C}$ .

### Total Simulated Rainfall for Days 4-10 ( $t = 72 - 240$ h)

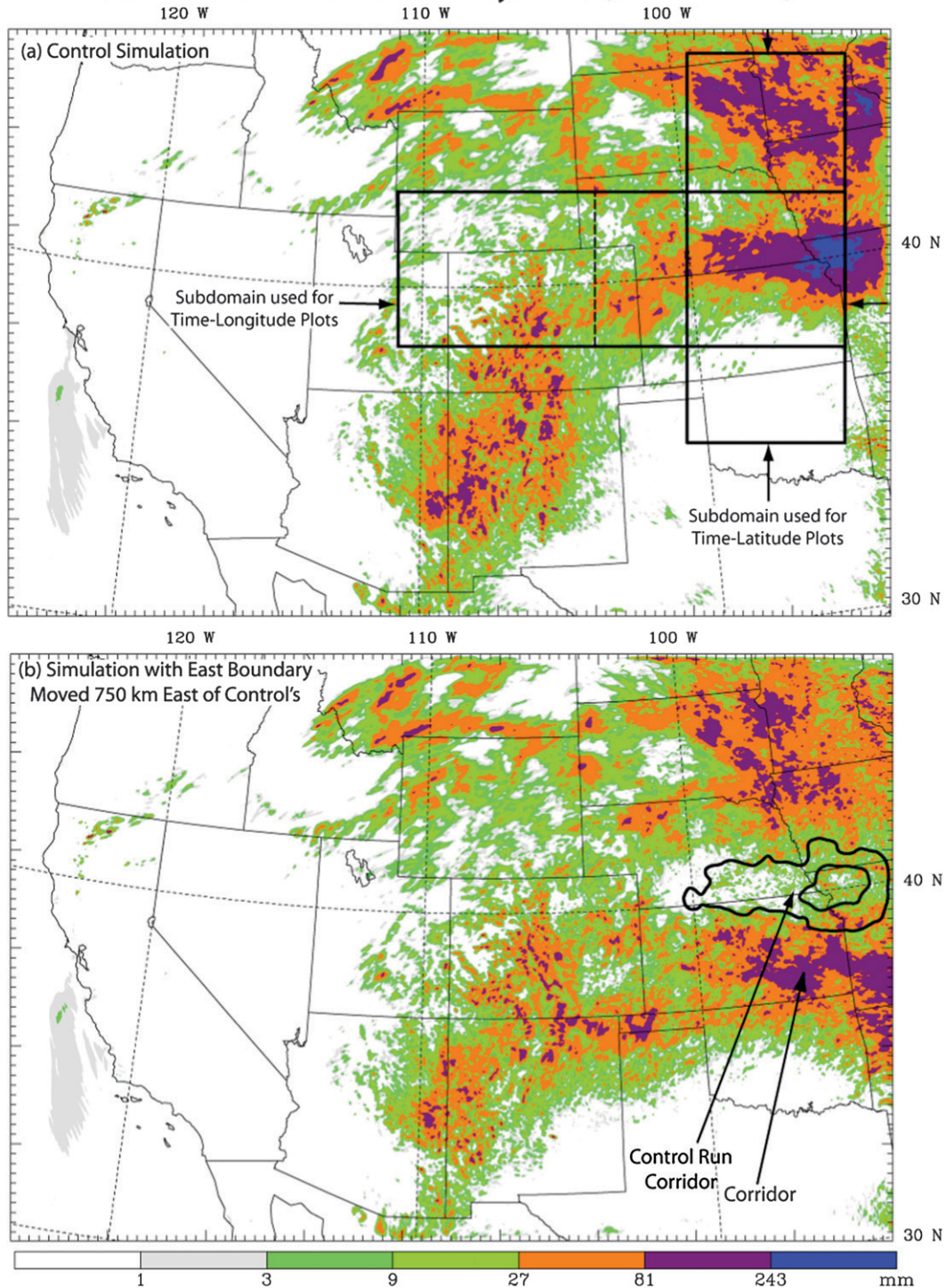


FIG. 4. Total rainfall (mm) for the final 7 days of (a) the control simulation and (b) a simulation where the eastern lateral boundary has been moved 750 km east of that shown in the plot. In (b) the location of precipitation exceeding 60 and 240 mm in the control run is overlaid to facilitate comparisons with this extended-domain simulation. In (a) the locations of  $x$ -averaged and  $y$ -averaged Hovmöller-type diagrams presented later are indicated by the solid bold rectangles. The dashed bold line in (a) indicates the western boundary of the portion of the  $x$ -oriented rectangle that encloses the plains rainfall corridor region for which area-averaged time series are presented in Fig. 5.

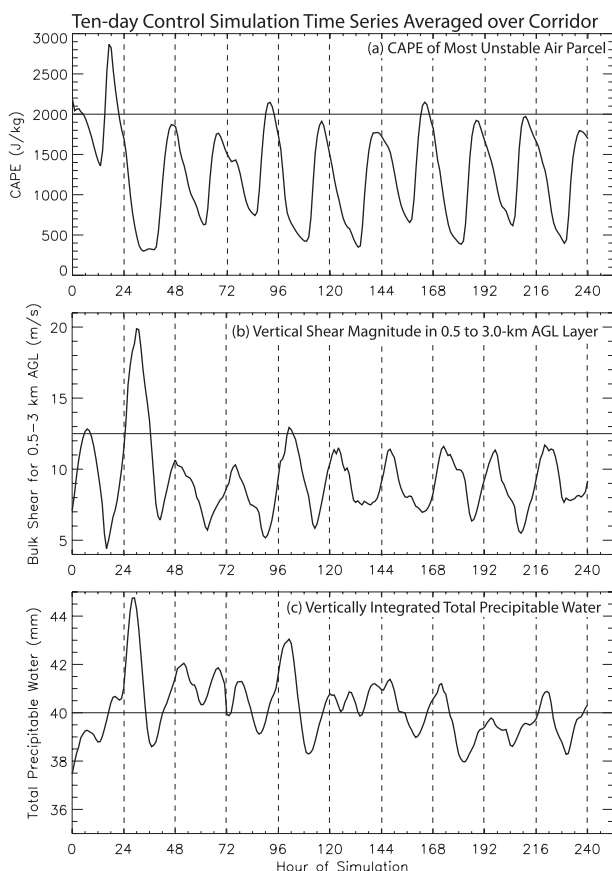


FIG. 5. Time series from the 10-day control simulation area averaged over the plains corridor region formed by the dashed bold line and the remaining (eastern) part of the solid bold  $x$ -oriented rectangle in Fig. 4a. (a) CAPE (defined as in Fig. 3b), (b) 0.5–3 km AGL vertical shear magnitude, and (c) total column water (including water vapor, cloud, and precipitation hydrometeors). The dashed vertical lines are for reference, indicating 0000 UTC ( $\sim$ 1800 LST).

scheme (Hong et al. 2004) that includes cloud water, cloud ice, rain, graupel, and snow categories and the Rapid Radiative Transfer Model longwave (Mlawer et al. 1997) and Dudhia (1989) shortwave radiation schemes.

Since WRF has a rigid upper boundary and we are analyzing simulations involving both deep convection and flow over a significant mountain cordillera, a 5-km-deep Rayleigh absorbing layer (Klemp et al. 2008) is used to effectively mitigate reflection of vertically propagating gravity waves off the model top. The use of a positive-definite advection scheme for water vapor and hydrometeors eliminates artificial sources of precipitation (Skamarock and Weisman 2009), which is crucial for realistic simulation of the water cycle over the central United States (section 7), where the heaviest rainfall occurs (Fig. 4a).

## b. Simulations and analysis procedures

In this paper we focus almost entirely on a single control simulation. However, several additional sensitivity simulations were conducted. These included a 10-day dry simulation that was configured identically to the control run except that no phase changes of water vapor were allowed. This simulation was useful to compare to the control simulation to help interpret some of the effects of convection on its environment. However, not surprisingly, the absence of deep convection during the multiday integration led to several unrealistic attributes including anomalously warm surface conditions and anomalously small tropospheric static stability that trended toward dry adiabatic in the interior of the domain. This run is only briefly discussed in the remainder of the paper. We also examined a simulation with control simulation parameters but an eastward-extended horizontal domain. This simulation is discussed briefly in section 4.

Our primary interest is on the macroscale aspects of the diurnal cycle of convection and its environment. To facilitate examination and discussion of these aspects, considerable use is made of displays that reveal temporally and or spatially averaged structures. These include area-averaged budgets, time and  $y$ -averaged  $x$ – $z$  vertical cross sections, and time–distance Hovmöller-type diagrams.

At least two days of model integration were required to achieve relatively steady diurnal cycle of parameters important to convection such as CAPE (Fig. 5a) and vertical shear (Fig. 5b). Thus, in the remainder of the paper we focus on analyses from 72 to 240 h (days 4–10) and on 7-day averages over this period. Note, however, that the model convection never reaches an exact “equilibrium” with its environment on diurnal time scales. This is evident from the daily variations in the maximum and minimum column integrated precipitable water (Fig. 5c).

## 4. The diurnal cycle of simulated precipitation

### a. Horizontal distribution of precipitation

The heaviest simulated precipitation during the final seven days of the simulation occurs over the mountains and continues in a narrow west–east-oriented CPL corridor centered near  $40^{\circ}\text{N}$  (Fig. 4a). This is a common midsummer precipitation pattern for which a similar example during July 1998 was illustrated in Carbone et al. (2002, see their Fig. 11).

A sensitivity experiment using a horizontal domain that extends 750 km eastward from the eastern lateral boundary of the control simulation also exhibits a plains heavy precipitation corridor. However, this corridor is weaker and centered  $\sim 2^{\circ}$  south at  $\sim 38^{\circ}\text{N}$  (Fig. 4b). The

differences between the simulations are traced back to an anomalously strong and long-lived MCS during  $t = 24\text{--}48$  h (Fig. 5), which marked the first large-scale convective response to the initial condition. In the control simulation the effect of this convection is minimized (perhaps fortuitously) by its earlier movement through the eastern lateral boundary than in the larger domain simulation. In contrast, the original MCS in the extended domain simulation persists beyond the eastern boundary of the control run, resulting in greater overall cold air production near the surface. This cold air is advected southwestward into the Great Plains and results in differences in the location of the surface frontal zone within which subsequent precipitation systems during the remainder of these two simulations track (not shown).

The more northward location of the control run precipitation corridor better matches the zone of maximum observed rainfall frequencies near  $40^\circ\text{N}$  (Fig. 2b). The greater intensity of this precipitation corridor is also consistent with more favorable environmental conditions for strong convection in this location than farther south, including stronger midtropospheric flow (and hence stronger vertical shear) and larger upstream CAPE in the monthly averaged observations (Fig. 3). Because of the greater realism of its heavy precipitation corridor location relative to both the monthly observed heavy precipitation corridor and the favorable large-scale environment, our forthcoming analysis of the simulated diurnal cycle focuses on the control run.

The diurnal cycle of precipitation begins near midday with mountain convection (Fig. 6b), which has maximum frequencies and coverage from late afternoon to early evening (Figs. 6c,d). This is followed by two well-defined latitudinal corridors of maximum frequency late at night over the plains (Fig. 6e). The southernmost corridor has maximum frequencies, is longest lasting, and coincides with the greatest overall precipitation during the simulation (Fig. 4a).

Both simulated corridors are well defined in time–latitude diurnal frequency diagrams (Fig. 7a) and have clear analogues in similar diagrams constructed from observations for the entire month of July 2001 (Fig. 2b)<sup>1</sup> despite the averaging used to create the initial and lat-

eral boundary conditions (section 3). The time–latitude hourly rain-rate Hovmöller diagram (Fig. 7b) reveals that while simulated rainfall occurs over the southernmost corridor every night, there are significant variations in intensity. This convection has latitudinal progression on some nights but overall has no clear preference for either northward or southward movement (Figs. 7a,b). In contrast, the northernmost corridor has a clear preference for southward movement of the precipitation within it (Figs. 7a,b). Hereafter, we concentrate on the southernmost corridor because it best typifies the mid-summer climatological situation of heavy rainfall occurring in an environment of shallow and relatively weak baroclinity.

#### *b. Eastward progression of rainfall during the diurnal cycle*

Simulated afternoon convection in the mountains is quasi-stationary as found in warm-season precipitation climatologies (e.g., Carbone et al. 2002; Carbone and Tuttle 2008). The eastward-progressing rainfall in the corridor region ( $38^\circ\text{--}42^\circ\text{N}$ ) commences east of  $\sim 105^\circ\text{W}$  during the late afternoon (Fig. 8a). This convection forms along west–east-oriented ridges in the immediate lee of the Rockies (Fig. 6c), as opposed to moving directly out of the mountains. Origins of observed progressive nocturnal MCSs over the southern Great Plains have similarly been traced to afternoon and evening convection along west–east-oriented ridges in the lee of the Colorado and New Mexico mountains (Hane et al. 2008).

In contrast to results from the current simulation, convection originating along the high peaks of the Rockies can progress eastward, leading to eventual MCS development (Cotton et al. 1983; McAnelly and Cotton 1989). In an idealized modeling study, Tucker and Crook (2005) found that the organization of mountain-generated convection onto the plains was highly dependent on the large-scale 500-hPa flow. In particular, they noted that weak westerly 500-hPa flow favored many convection initiation sites in the mountains but inhibited movement of this convection onto the plains, consistent with the current modeling results (cf. Fig. 3a).

For convection originating in the lee of the Rockies, only that generated along the Palmer Divide in central Colorado is able to persist long enough into the evening to contribute to the onset of the nocturnal precipitation corridor (Fig. 6d) in the current simulation. Environmental factors favoring the persistence and growth of this afternoon convection are detailed in section 6.

This precipitation, which originates during the afternoon near  $\sim 105^\circ\text{W}$ , progresses eastward to  $\sim 98^\circ\text{W}$  by late evening and exhibits coherence in the time–longitude rainfall frequency diagram with a phase speed of  $\sim 16$  m  $\text{s}^{-1}$

<sup>1</sup> The Hovmöller-type diagrams for the simulation were constructed directly from  $x$ – $y$  model grid output avoiding any spatial interpolation. However, to facilitate comparisons with observations (Figs. 1 and 2), the model data are displayed with approximate latitude or longitude as the horizontal coordinate. Here, the longitude or latitude value is the average for the  $x$  or  $y$  model grid point over which the fields are averaged. The distortions of  $1.5^\circ$  lon ( $0.5^\circ$  lat) between endpoints in time–latitude (–longitude) Hovmöller plots of the simulation are minor enough not to affect conclusions drawn from these analyses.

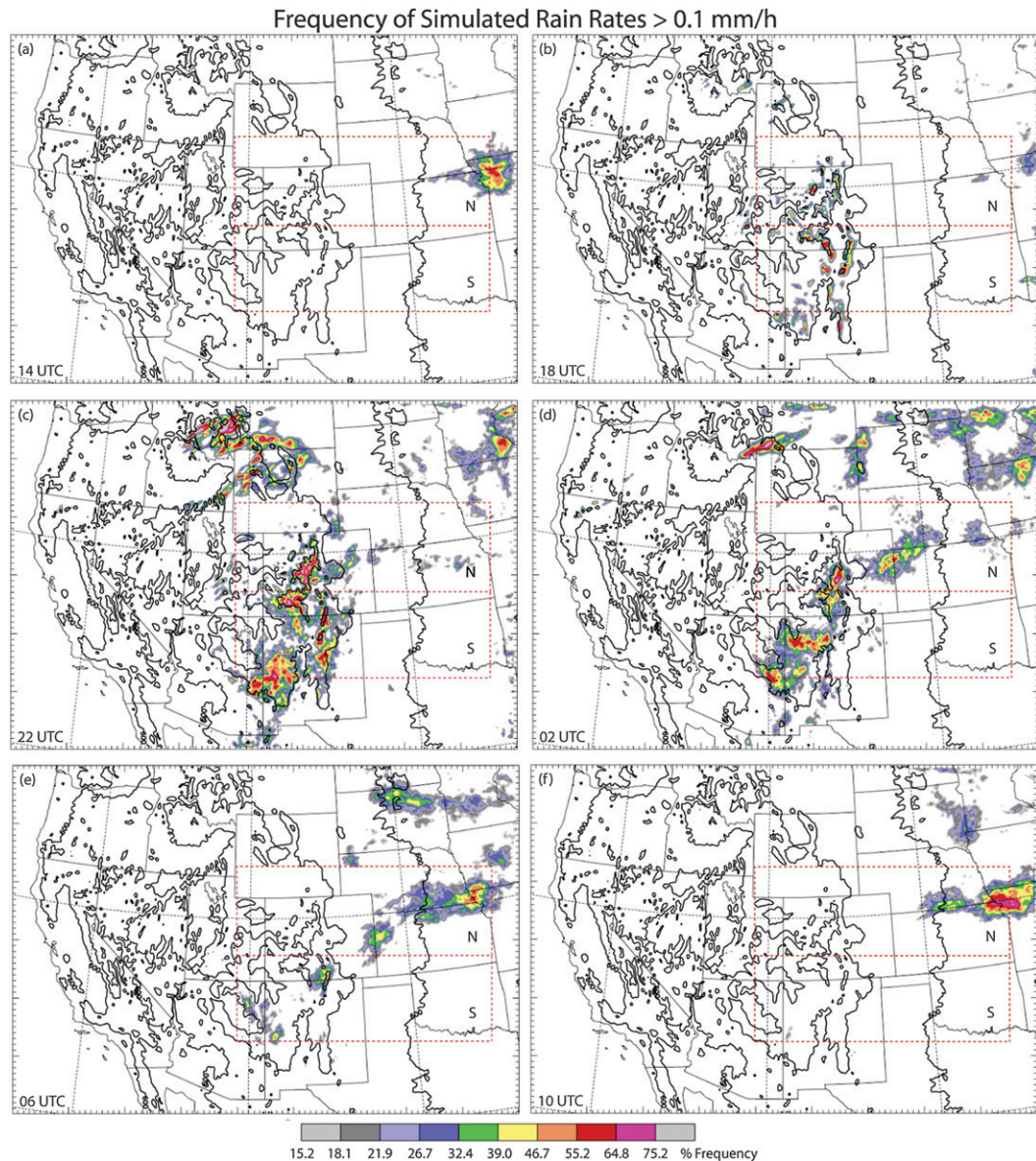


FIG. 6. Diurnal frequency plots of hourly rain rate in the control simulation exceeding  $0.1 \text{ mm h}^{-1}$  constructed using 3-h centered means for the 7-day period. The dashed red rectangles N and S refer to the location of the  $y$ -averaged  $x$ - $z$  cross sections presented in Fig. 9. Bold contours represent terrain heights in intervals of 600 m.

(Fig. 8a). This behavior is broadly consistent with the observations from July 2001 (Fig. 2a) and climatologies of precipitation episodes (Carbone et al. 2002; Carbone and Tuttle 2008).

The attribute of the simulated precipitation that differs most substantially from the July 2001 observations is the lack of continuous eastward progression of individual rain streaks beyond  $98^\circ\text{W}$  (central Kansas) (Fig. 8b), which are most pronounced in the observations during the second half of the month (Fig. 1a). Here, the model initial conditions derived from the July 2001 average (Fig. 3) may not represent conditions that favor the

longest-lived rain streaks. This could result from both meridional shifts in environmental conditions most favorable for heavy precipitation corridors and inclusion of days less favorable for continuous eastward progression during this period. The large-scale initial conditions also do not contain significant midlevel short waves often associated with long-lived continuously propagating convection events (e.g., Johns and Hirt 1987; Trier et al. 2006).

Although some rain streaks with large zonal spans ( $L < 1000 \text{ km}$ ) occur in the simulation (Fig. 8b), there are also many nights with multiple shorter-lived eastward-progressing rain streaks that redevelop at roughly the

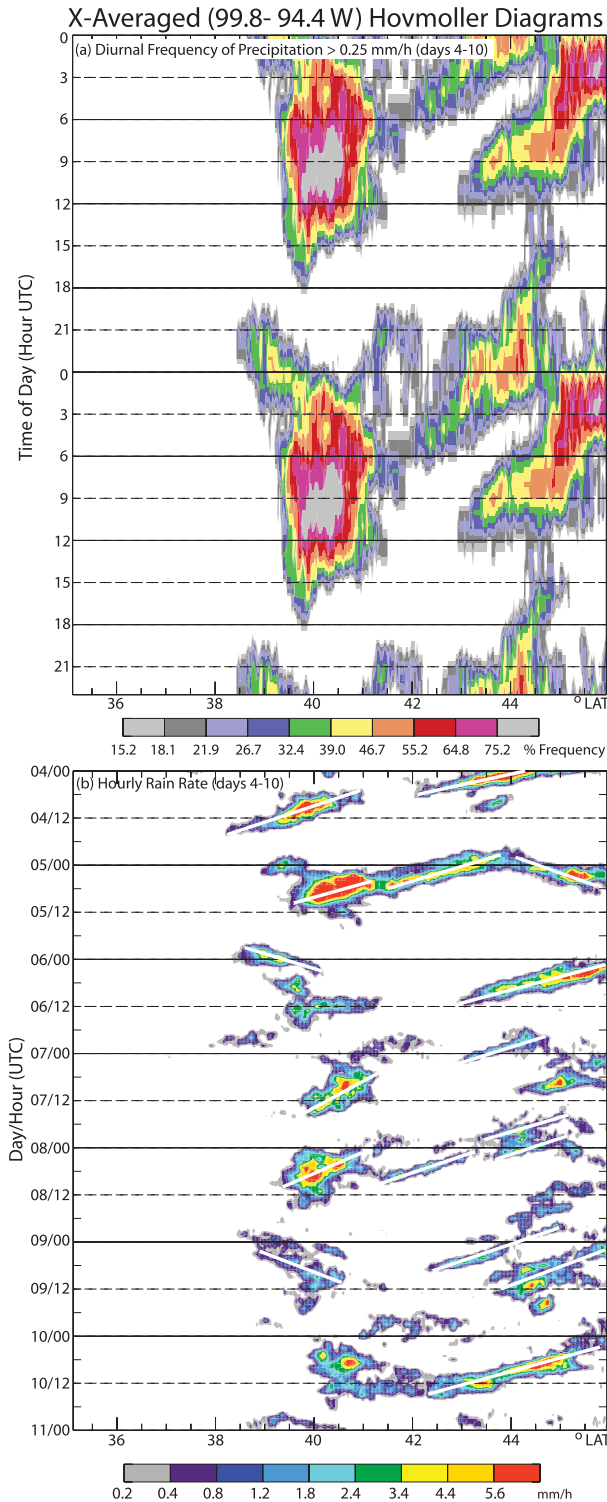


FIG. 7. The x-averaged Hovmöller diagrams for simulation days 4–10 of (a) diurnal frequency of rainfall averaged over the approximate 99.8°–94.4°W longitude band exceeding 0.25 mm h<sup>-1</sup> (constructed using 3-h centered means) and (b) average rain rate (mm h<sup>-1</sup>) over the approximate 99.8°–94.4°W longitude band. The white lines in (b) indicate rain streaks persisting for more than 3 h with average rain rate exceeding 0.25 mm h<sup>-1</sup>.

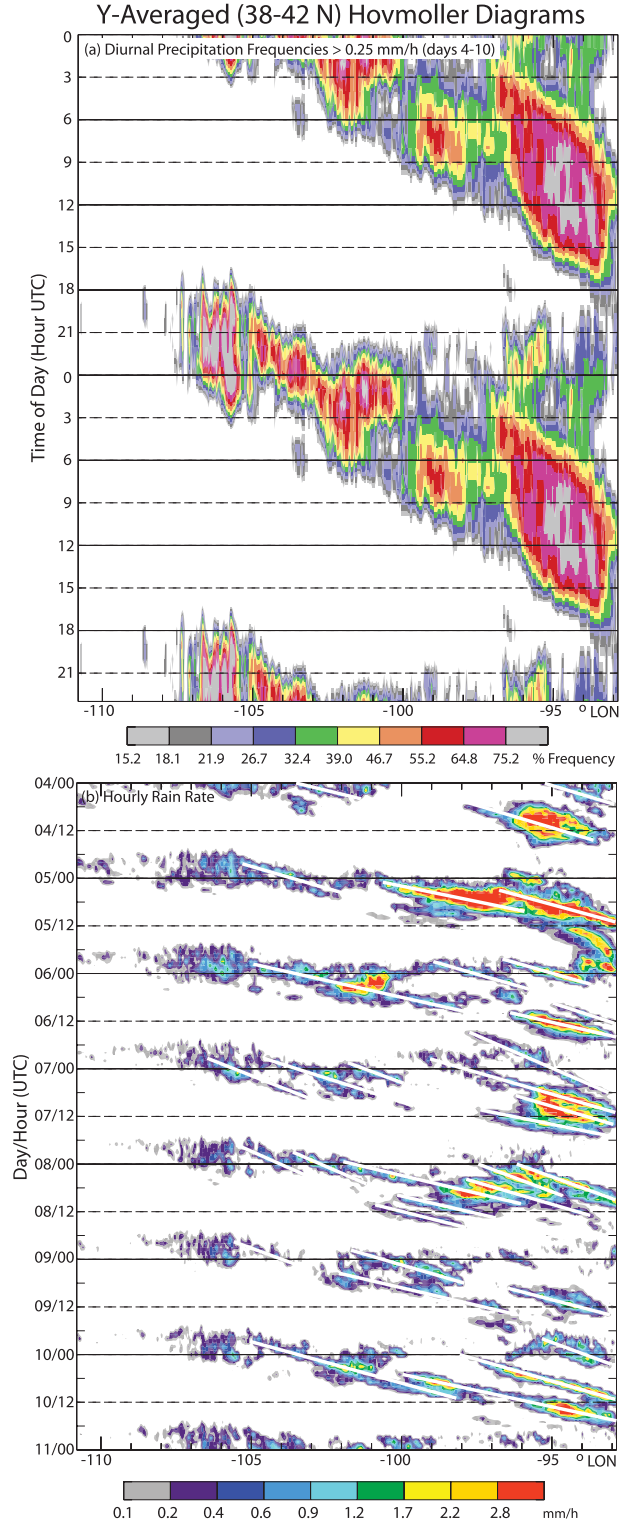


FIG. 8. The y-averaged Hovmöller diagrams for simulation days 4–10 of (a) diurnal frequency of rainfall averaged over the approximate 38°–42°N latitude band exceeding 0.25 mm h<sup>-1</sup> (constructed using 3-h centered means) and (b) average rain rate (mm h<sup>-1</sup>) over the approximate 38°–42°N latitude band. The white lines in (b) indicate rain streaks persisting for more than 3 h with average rain rate exceeding 0.25 mm h<sup>-1</sup>.

## 7-Day Averaged Mountain-Plains X-Z Circulation

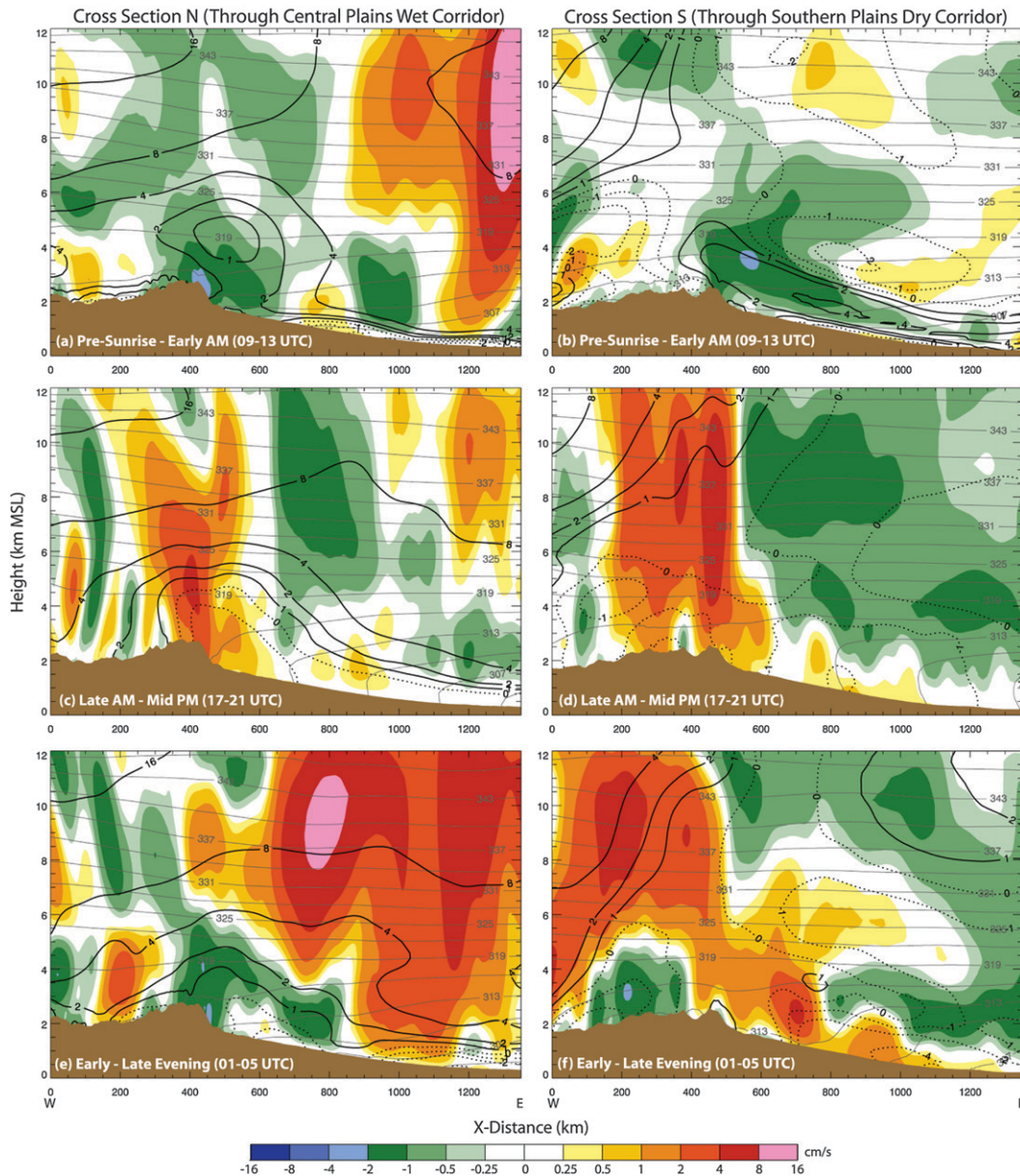


FIG. 9. Seven-day time-averaged  $x$ - $z$  cross sections of vertical velocity (color scale),  $x$ -wind component (nonzero values starting at 1 and  $-1$  with contour intervals in multiples of 2; zero and negative values dashed), and potential temperature (3-K contour intervals) from the control simulation, which are averaged in the  $y$  direction for 450 km. The cross sections are derived from 4-h time averages of the control simulation over the (a),(c),(e) north “N” and (b),(d),(f) south “S” dashed rectangular regions in Fig. 6 for 0900–1300, 1700–2100, and 0100–0500 UTC, respectively. The solid brown at the base of each panel represents the mean  $y$ -averaged terrain.

same longitude or even successively westward (e.g., days 7 and 8). The overnight redevelopment of convection contributes to both an enhancement of maximum rainfall frequency and steeper slopes (i.e., slower eastward progression) of the largest rainfall frequencies around  $95^{\circ}\text{W}$  compared to those associated with convection that

originates earlier and closer to the Rockies (Fig. 8a). Observationally based climatological studies of heavy precipitation corridors have similarly used diurnal frequency diagrams to suggest that redeveloping or locally forced nocturnal convection may significantly augment precipitation from continuously progressing convection

7-Day Averaged 19 UTC Low-Midtropospheric Conditions in the Lee of the Rockies

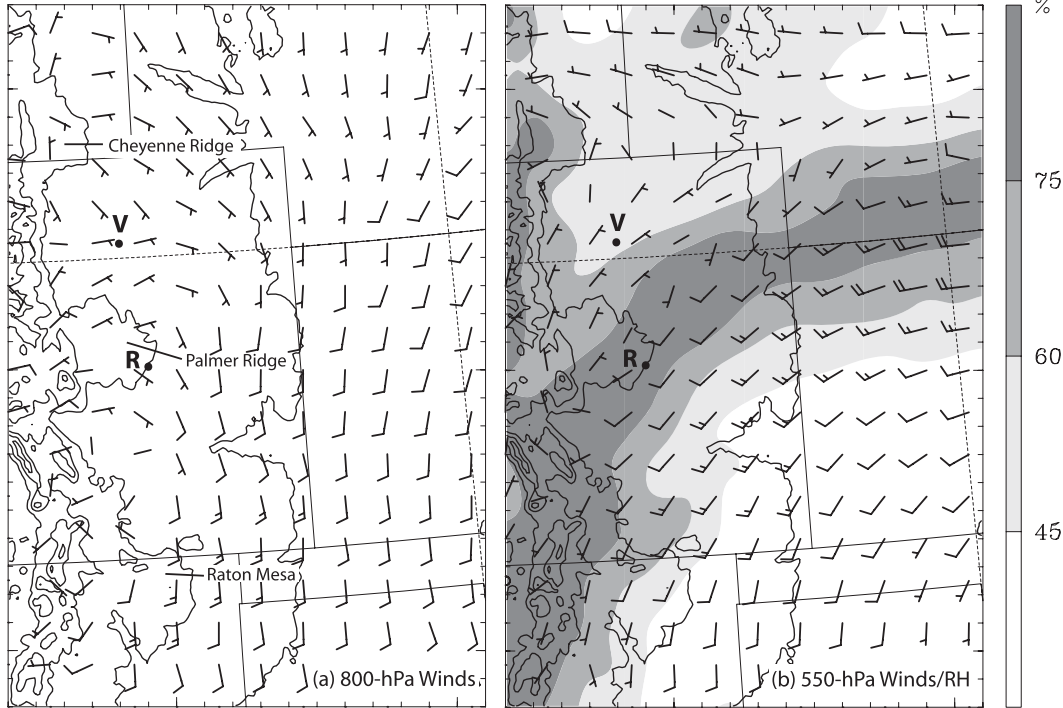


FIG. 10. (a) 800-hPa wind and (b) 550-hPa wind and relative humidity (shading) at 1900 UTC derived from 7-day averages of the control simulation. The bold contours in each panel indicate terrain increments of 300 m. Points R and V refer to the ridge and valley locations of coincident soundings plotted in Fig. 11. The annotated features in (a) refer to west–east-oriented features of elevated terrain situated immediately east of the Rockies.

initiated earlier and well upstream (Tuttle and Davis 2006, their Figs. 4d and 9d). In section 6 we discuss environmental conditions leading to this behavior in the control run.

**5. Mountain–plains circulation and its relationship to the diurnal cycle of precipitation**

The most general aspect of simulated diurnal frequencies of precipitation (Figs. 7a and 8a) supported by observations (Figs. 2a,b) is the shift from daytime precipitation over the mountain cordillera to the adjacent Great Plains at night. Wang and Dai (2009, manuscript submitted to *Geophys. Res. Lett.*) used the North American Regional Reanalysis (Mesinger et al. 2006) to document the thermally driven mountain–plains circulation, which model-based studies (e.g., Tripoli and Cotton 1989a,b; Koch et al. 2001) have also illustrated as a mechanism supporting this aspect of the regional daily warm-season precipitation cycle.

We examine this circulation using vertical cross sections of 7-day-averaged vertical velocity, potential temperature, and zonal wind component along  $y$ -averaged west–east vertical cross sections defined by the dashed

rectangles in Fig. 6. These 7-day-averaged cross sections are derived from hourly model output and are averaged further over 4-h periods to represent distinct phases of the diurnal cycle. Prior to temporal and zonal averaging we apply the scale selective filter used by Barnes et al. (1996),

$$F(x, y) = \left[ \frac{\sin(\pi x/D)}{(\pi x/D)} \right] \left[ \frac{\sin(\pi y/D)}{(\pi y/D)} \right], \quad (1)$$

to these three-dimensional fields at each grid point on constant pressure surfaces with  $D = 60$  km to emphasize mesoscale and greater wavelengths.

Important differences are found among the cross sections extending eastward from the mountains into the CPL nocturnal precipitation corridor (Figs. 9a,c,e) and those located to the south (Figs. 9b,d,f). Prior to significant solar heating, the south cross section exhibits a shallow well-defined circulation cell centered at  $x = 800$  km (Fig. 9b) consistent with nocturnal cooling of the slope under dry conditions. Subsidence in the immediate lee of the mountains also occurs in north cross section (Fig. 9a). However, here the circulation is

complicated by stronger background westerly flow over the mountains (cf. Fig. 3a) and domination by the nocturnal MCS circulation (cf. Figs. 6a,f) east of  $x = 850$  km (Fig. 9a).

The vertical circulations within these cross sections are most similar during the period from late morning through midafternoon (Figs. 9c,d). By this time surface heating over the mountain cordillera and adjacent slope has driven a flow reversal from early morning with upslope flow now occurring in the lee of mountains. The deep tropospheric ascent over the mountains with deep subsidence above the PBL over the plains to the east suggests that by this time the thermally driven circulation has begun to couple with a deep convective circulation as described by Tripoli and Cotton (1989a). The mean daytime subsidence over the plains is generally stronger and more widespread in the south cross section (Fig. 9d) and thus may be more effective in suppressing convection in this region than over the nocturnal precipitation corridor to the north (Fig. 6c). Possible factors influencing the stronger subsidence in the south cross section include 1) compensation for stronger net upward mass flux in the more widespread and frequent convection over the southern Rockies (Figs. 6b,c) and 2) stronger synoptic-scale forcing for descent resulting from proximity to the midlevel anticyclone center (Fig. 3a).

One exception to the stronger late morning–early afternoon subsidence over the plains in the south cross section is the locally enhanced subsidence immediately above the shallow PBL toward the east edge (near  $x = 1200$  km) of the north cross section (Fig. 9c). Here, the enhanced subsidence is surmounted by upper-level ascent suggesting possible influences from weak residual circulations associated with the decayed antecedent MCS activity (Figs. 6a,b).

By evening the vertical motion patterns in the north and south regions are almost completely out of phase (Figs. 9e,f). In the north cross section strong low to midtropospheric descent has developed over the high terrain and its lee as upward motion associated with organizing nocturnal convection has developed over the plains (Fig. 9e). In contrast, mountain convection persists several hours later over southern Colorado and New Mexico (Fig. 6d). This is reflected by continued ascent over the mountains with upslope flow in the lee persisting well into the evening in the south cross section (Fig. 9f). The pronounced differences in vertical circulation and persistence of convection between northern and southern mountain locations could be a response to concurrent differences in the onset of highly organized nocturnal convection over the adjacent plains. However, confirmation of this possibly requires further investigation with an idealized model.

### 7-Day Averaged 19 UTC Soundings in Lee of the Rockies

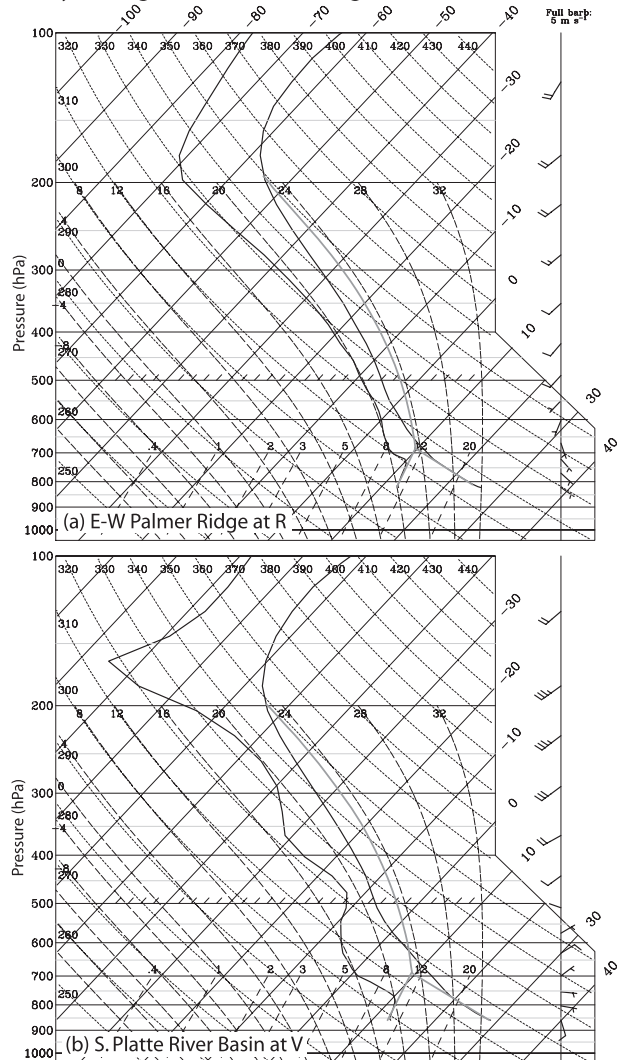


FIG. 11. Seven-day-averaged early afternoon (1900 UTC) control simulation vertical soundings of temperature, dewpoint, and horizontal wind from locations (a) R along west–east-oriented Palmer Ridge and (b) V in the South Platte River Basin indicated in Fig. 10. Gray curves indicate ascent paths predicted by parcel theory for air parcels of average potential temperature and water vapor mixing ratio from the lowest 500 m AGL.

## 6. Factors influencing localization and eastward progression of precipitation within the latitudinal corridor

### a. Daytime initiation of convection within the corridor

Mean lower tropospheric ascent associated with the mountain–plains solenoid characterizes the longitudinal band in the immediate lee of the Rockies (Fig. 9c) where eastward-progressing convection begins. However, there is considerable meridional variation that helps localize

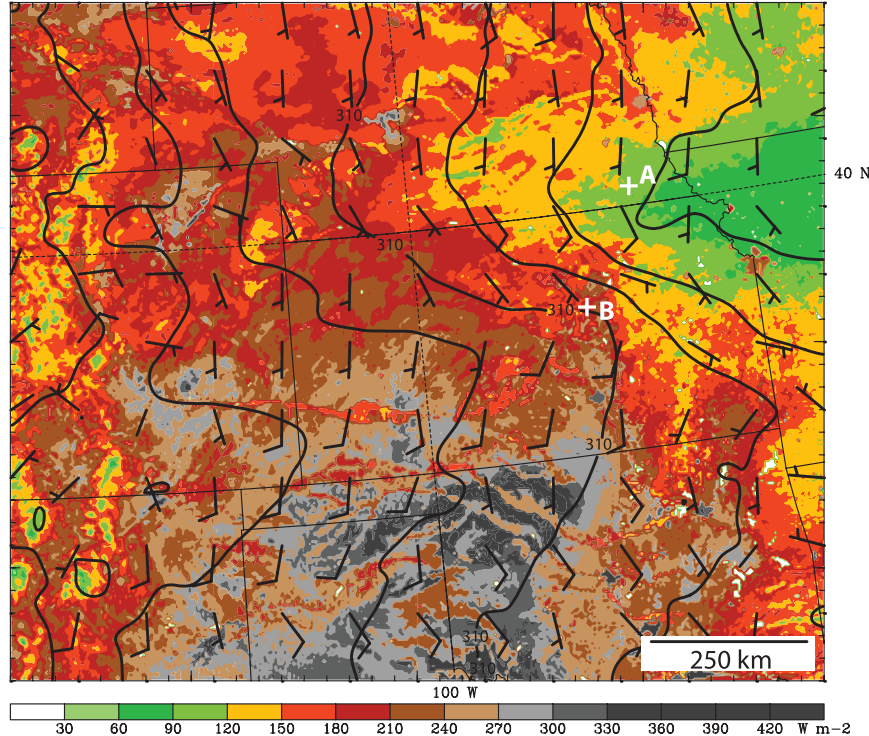
7-Day Averaged Surface Sensible Heat Flux (14–20 UTC) and  $\theta$ , Winds (18 UTC)

FIG. 12. Seven-day-averaged 1400–2000 UTC surface sensible heat flux (color scale) and 1800 UTC surface potential temperature analysis (2.5-K contour intervals) with horizontal wind from the control simulation. Locations A and B denote positions of soundings in Fig. 13.

the convection initiation along the west–east-oriented ridges (Fig. 6c). The 7-day-averaged simulated early afternoon PBL flow (Fig. 10a) indicates convergence along the west–east-oriented ridges and divergence in between. This flow pattern is quite similar to that obtained by Toth and Johnson (1985) from monthly averaged surface mesonet data for July 1982 (their Fig. 2e).

A comparison of 7-day-averaged 1900 UTC soundings reveals a small range of CAPE from  $\sim 1200 \text{ J kg}^{-1}$  at point R along the Palmer Divide (Fig. 11a) to  $\sim 1100 \text{ J kg}^{-1}$  at point V in the South Platte River Basin (Fig. 11b) but more substantial differences in susceptibility to convection. Unlike at point R (Fig. 11a), there is both low-level divergence (Fig. 10a) and a deep layer of negative buoyancy for surface-based air parcels with dry conditions immediately above the PBL (Fig. 11b) inhibiting convection at point V.

Midtropospheric conditions are also especially moist at point R (Fig. 10b). The midlevel moisture is embedded within southwesterly flow and thus extends significantly eastward into the nocturnal precipitation corridor where it approximately coincides with a surface baroclinic zone (Fig. 12). Together these factors provide a focus that allows eastward moving convection originat-

ing along or near the Palmer Divide to persist significantly longer than convection originating on west–east ridges to the north and south (Figs. 6c,d). It is this convection that evolves to compose early stages of nocturnal precipitation within the latitudinal corridor.

The paucity of daytime convection farther east is consistent with the weak zonally averaged subsidence discussed in the previous section (Fig. 9c). The location of what little afternoon convection occurs (Fig. 6c) can be explained by meridional differences in conditions across the surface front (Fig. 12), which itself is influenced by the repetitive nature of nocturnal convection within the latitudinal corridor. Here, the time-integrated (1400–2000 UTC) sensible heat flux occurring at point A in the wake of nocturnal and early morning convection is considerably less than farther south at point B near the leading edge of the surface front.

The average midafternoon sounding at point A (Fig. 13a) has substantial CAPE of  $\sim 2200 \text{ J kg}^{-1}$  but contains a deep and significant layer of negative buoyancy above its shallow PBL that contributes to convective inhibition (CIN) of  $\sim 50 \text{ J kg}^{-1}$ . The significant CIN, which delays convection, is influenced not only by subsidence (Fig. 9c) but also by limited sensible heating

## 7-Day Averaged 21 UTC Soundings for E-W Precip Corridor

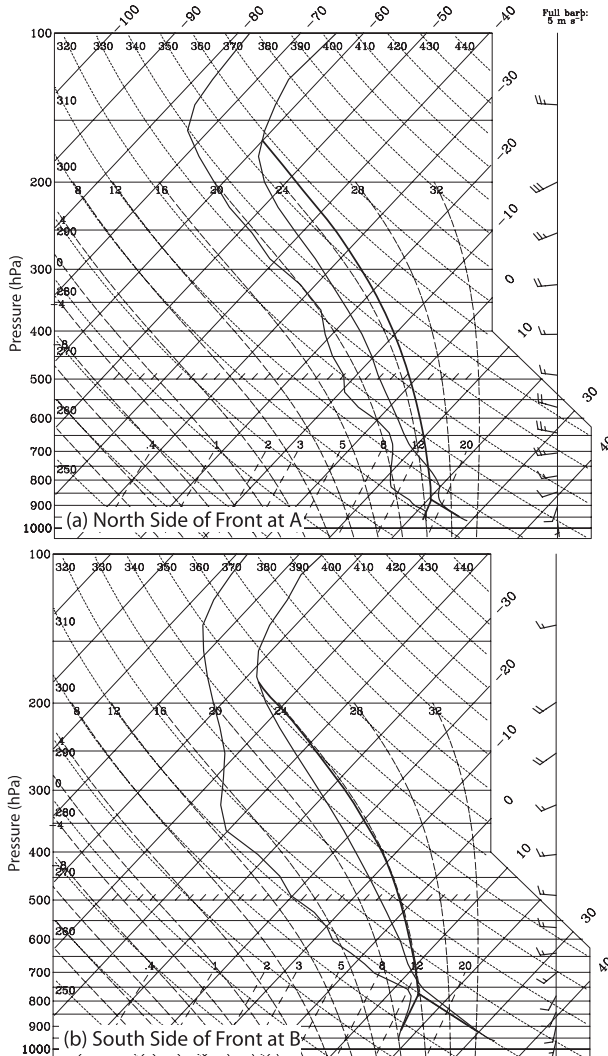


FIG. 13. As in Fig. 11, but at 2100 UTC and for the locations A and B situated, respectively, north of and at the southern edge of the 7-day-averaged quasi-stationary front depicted in Fig. 12.

that restricts PBL growth in the wake of nocturnal convection. The much stronger sensible heating at the southern edge of the front at point B, where it does not rain overnight, results in a deeper midafternoon PBL (Fig. 13b). The more vigorous vertical mixing is partly responsible for lesser average CAPE of  $\sim 1400 \text{ J kg}^{-1}$  but it also contributes to negligible average CIN of  $< 10 \text{ J kg}^{-1}$ , which allows late afternoon convection to form near the south end of the front on some days, despite the more general subsiding layer above the PBL (Fig. 9c). This afternoon convection (near  $39^\circ\text{N}$  in Fig. 7a) is short lived and typically does not evolve upscale, consistent with the lack of strong vertical shear (Fig. 13b).

*b. Environmental factors governing the eastward-progressing nocturnal convection*

In contrast, significant increases in vertical shear occur during the evening, with maximum shear values found near the onset of maximum rainfall frequencies in the southern precipitation corridor (Fig. 14a). This evening trend in vertical shear magnitude contrasts with that of the maximum equivalent potential temperature  $\theta_e$  (Fig. 14b). Here, the out-of-phase relationship between maximum thermodynamic instability and maximum precipitation frequency points to the importance of dynamical mechanisms in organizing convection. As noted in the introduction, such mechanisms are often internal to the convection but may also be related to the evolving environment.

Observational studies of the environments of organized warm season convection typically emphasize importance of lower-tropospheric forcing on the mesosynoptic scale. One aspect of lower-tropospheric forcing that has received particular attention is the nocturnal LLJ, which results from a sudden reduction in eddy viscosity due to nocturnal PBL stabilization (Blackadar 1957) and is localized over the Great Plains because of the enhanced pressure gradient force that arises prior to its onset from the heating of sloped terrain (e.g., Holton 1967). It is through this latter mechanism that the LLJ is linked to the MPS circulation. The recent simulations of Jiang et al. (2007) have indicated that the effects of PBL stabilization and daytime heating of sloped terrain are of comparable importance to nocturnal LLJ development.

Maddox (1983) discussed the role of ascent implied by low-level warm advection by the nocturnal LLJ in development of mesoscale convective complexes (MCCs). Augustine and Caracena (1994) noted further that the mesoscale lower-tropospheric environment was highly frontogenetic in cases of stronger MCCs. Johns and Hirt (1987) stated that warm advection in the vicinity of a west–east-oriented surface front was a key ingredient in the environment of progressive (i.e., eastward translating) severe wind producing derecho MCCs, but they also noted that progressive midtropospheric geopotential height or vorticity perturbations were often present as well. We now examine the association of both midlevel and LLJ-related lower tropospheric forcings with large nocturnal precipitation frequencies in the current simulation.

### 1) MIDTROPOSPHERIC PERTURBATIONS

By experiment design, transient midtropospheric disturbances that enter the domain through the lateral boundaries are nearly eliminated. However, there is midtropospheric relative vorticity and PV due to both the initially prescribed quasi-stationary large-scale pattern

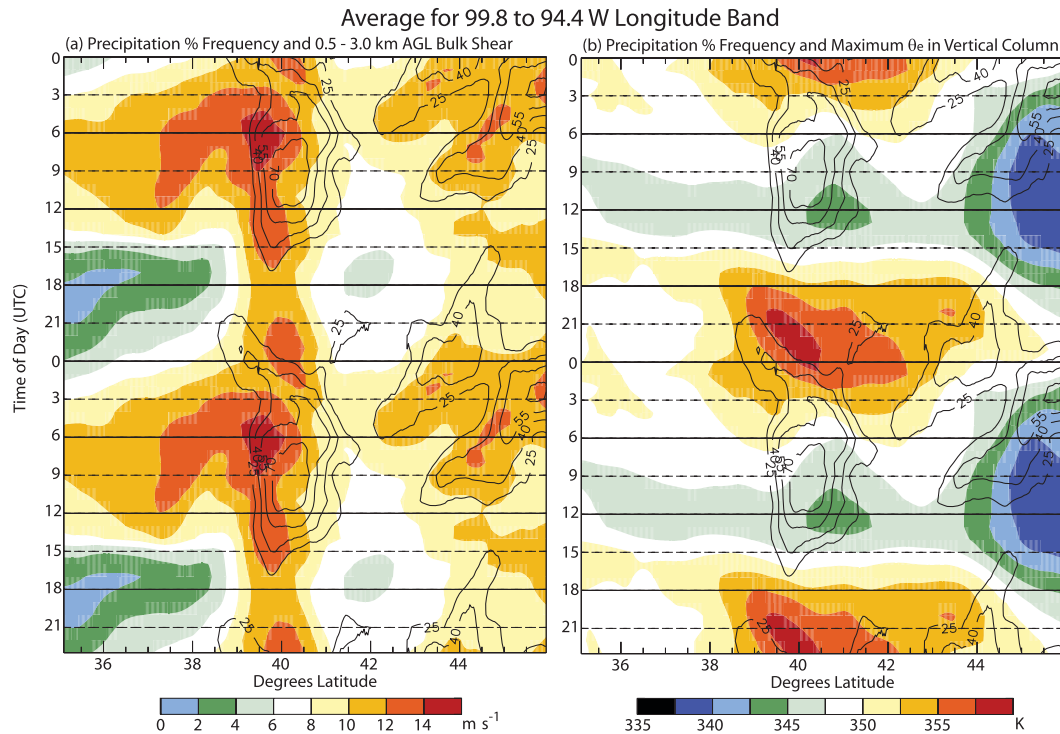


FIG. 14. Hovmöller diagrams averaged for the  $98.8^{\circ}$ – $94.4^{\circ}$ W longitude band of (a) 7-day-averaged magnitude of the 0.5–3.0 km AGL vertical shear vector (color scale) and (b) 7-day-averaged maximum equivalent potential temperature in a vertical column. Contour plots in (a) and (b) are a smoothed version of the more detailed diurnal frequencies of precipitation depicted in Fig. 7a.

and the internally generated structures resulting from a variety of mechanisms including deep convection, radiative heating of the topography, and the interaction of the large-scale flow with topography.

Figure 15a superposes the 7-day-averaged 650–500-hPa Ertel PV,  $\rho^{-1}(\zeta + 2\Omega) \cdot \nabla\theta$ , with precipitation frequencies in a diurnal time–longitude diagram. Here, we have subtracted the daily mean PV at each location prior to averaging since we are interested in isolating any phase-coherent part of the signal that could be related to the eastward-progressing precipitation signal. The most pronounced enhancement of PV occurs in the early morning in association with the large precipitation frequencies near  $\sim 95^{\circ}$ W overnight where its generation is an indication of midlevel circulation developing during the mature-to-dissipating stages of MCS convection.

Raymond and Jiang (1990) used a nonlinear balance model to explain how such circulations that arise from vertical gradients of diabatic heating within MCSs can help organize and sustain the large precipitation systems as they interact with the baroclinic environment. Examination of the relationship between rainfall and the full PV (Fig. 15b) suggests that the impact of such balanced dynamics may vary significantly over different

nights of the simulation. For example, on day 5 when a particularly long-lived and intense coherent rain streak occurs there is significant PV enhancement during much of its life cycle, as indicated by the yellow, orange, and red colors in Fig. 15b. This enhancement contributes to downshear redevelopment of convection near 1200 UTC on Day 5 (Fig. 15b). However, on most other nights significant midlevel PV enhancements do not occur until after the majority of the rainfall has ended, suggesting a lesser role in its diurnal cycle.

Also evident in Fig. 15b are weaker-amplitude variations of PV that begin near the lee of the Rockies and progress slowly eastward, maintaining coherence across the remainder of the model domain. These features exhibit diurnal periodicity with the positive PV perturbation reaching the CPL (e.g.,  $97^{\circ}$ W) near 0000 UTC the next day,  $\sim 24$  h after their onset (Fig. 15a). The maximum nocturnal rainfall frequencies east of this longitude occur approximately along the phase line of the positive PV perturbation (Fig. 15a), suggesting the possible role of the latter in focusing convection. However, both the weak amplitude of these features and their inability to excite deep convection upstream during the afternoon point toward additional factors (including the phase of

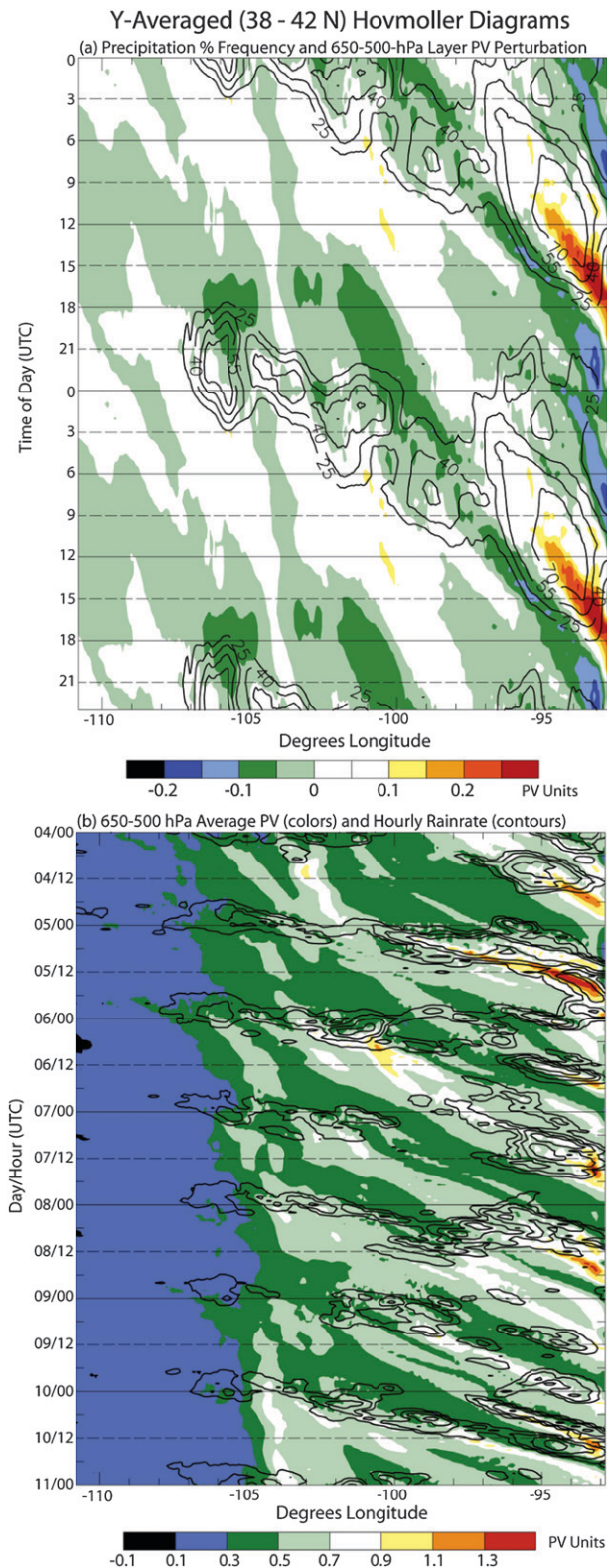


FIG. 15. The  $y$ -averaged Hovmöller diagrams from the control simulation. (a) Smoothed  $\sim 38^{\circ}$ – $42^{\circ}$ N latitudinally averaged diurnal frequency of rain rate exceeding  $0.25 \text{ mm h}^{-1}$  and 7-day

the MPS and the LLJ) as more important controls on deep convection in this region.

## 2) NOCTURNAL LLJ-RELATED FORCING

The LLJ can influence deep convection by enhancing warm advection in the frontal zone (Figs. 16a,c,e) and by influencing the vertical shear (Figs. 16b,d,f); both mechanisms can help convection organize upscale. Overnight, propagation associated with the nightly variation of LLJ intensity and direction becomes a factor contributing to the slower eastward progression of maximum diurnal frequencies east of  $\sim 98^{\circ}\text{W}$  (Fig. 8a). This propagation occurs when the forcing for new convective development departs significantly in direction from that of the mean flow. Case studies (e.g., Trier and Davis 2002; Schumacher and Johnson 2008) have illustrated excessive local rainfall amounts associated with MCS “back building” when the propagation vector is of nearly equal magnitude and is directed approximately antiparallel to the mean flow vector (Chappell 1986).

The process of MCS back building is illustrated by briefly examining an example case of nocturnal convection from the simulation. We select day 8 because this period exhibits the most striking example of westward redevelopment of eastward-progressing rain streaks (Fig. 8b). In this example (Fig. 17), the MCS leading edge (feature 1) progresses eastward while new convection clusters (features 2–4) originate successively westward. Although the newer clusters individually move eastward, their successive development results in a westward broadening of the precipitation envelope overnight (Figs. 8b and 17, day 8).

In the back-building MCS the vertical shear and warm advection play different roles in MCS organization in different locations and at different stages of the MCS life cycle. In the analysis that follows we examine the MCS structure by looking at vertical cross sections (Fig. 18) that are broad averages taken over different regions (Fig. 17). Similar to results from previous simulations of MCSs (e.g., Bernardet and Cotton 1998), this analysis reveals a transformation from an MCS driven primarily by dynamics at the leading edge of a cold pool to one governed by processes dependent on the evolution of the nocturnal LLJ within a broad baroclinic zone.

←

$\sim 38^{\circ}$ – $42^{\circ}$ N latitudinally averaged 650–500-hPa layer mean potential vorticity perturbation from the daily mean. (b) Day 4–10 smoothed  $\sim 38^{\circ}$ – $42^{\circ}$ N latitudinally averaged hourly rain rate with contours of 0.2, 0.6, 1.4, and  $3.0 \text{ mm h}^{-1}$  and  $\sim 38^{\circ}$ – $42^{\circ}$ N latitudinally averaged 650–500-hPa layer mean potential vorticity. An unsmoothed version of the contoured field in (b) is shown in Fig. 8b.

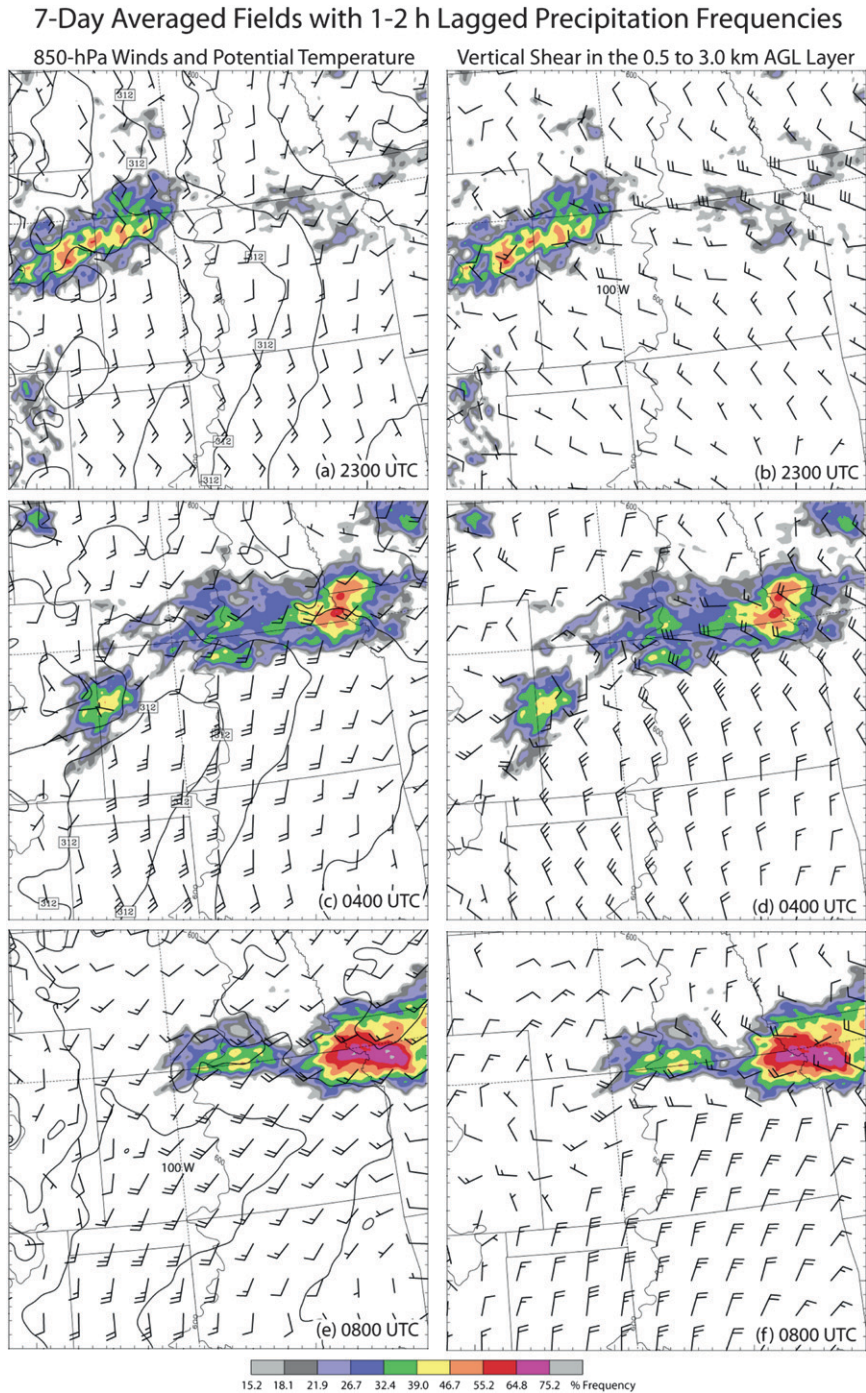


FIG. 16. Seven-day-averaged 850-hPa horizontal wind and potential temperature analysis (2-K contour intervals) from the control simulation for (a) 2300, (c) 0400, and (e) 0800 UTC. Seven-day-averaged wind difference vector (vertical shear) from 0.5 to 3.0 km AGL from the control simulation for (b) 2300, (d) 0400, and (f) 0800 UTC. Frequencies of hourly rain rate exceeding  $0.1 \text{ mm h}^{-1}$  (constructed using 3-h means) are superposed in each panel for the 1- to 2-h time interval following the plotted conditions.

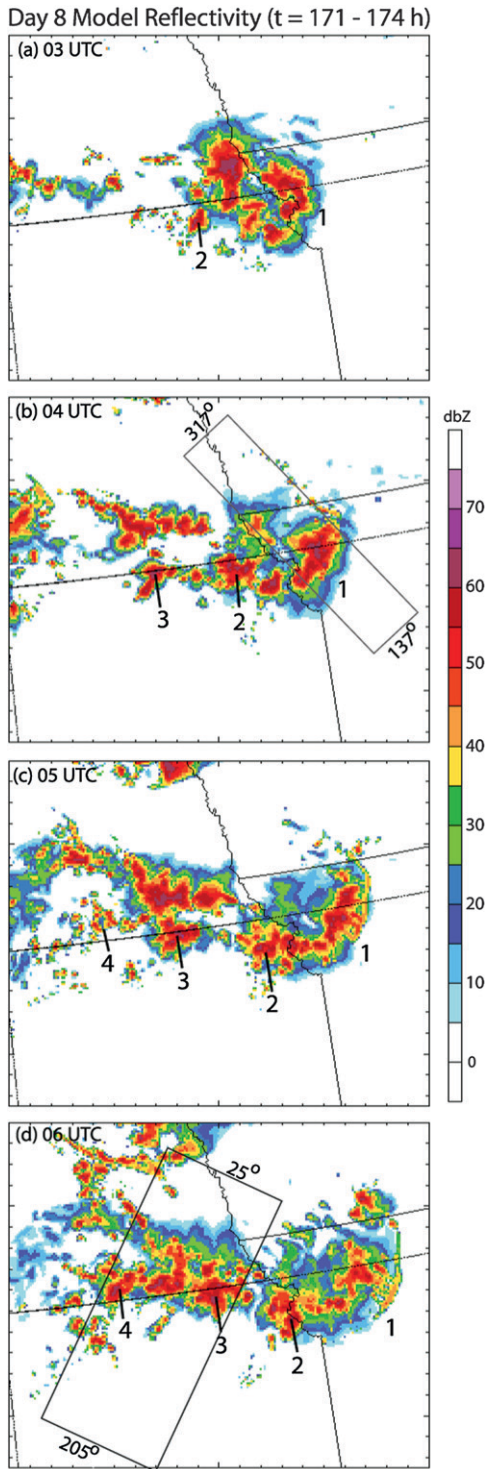


FIG. 17. Maximum model reflectivity in a vertical column for an example of westward developing (back-building) convection on day 8 of the control simulation. The annotated feature 1 marks the southeast edge of active convection within the eastward-advancing MCS. Additional annotated features indicate selected eastward-moving convective clusters that develop successively westward from 2 through 4. The transect in (b) [(d)] locates the vertical cross section of Fig. 18a (Fig. 18b) taken through the southeast (southwest) flank of the MCS at 0400 (0600) UTC.

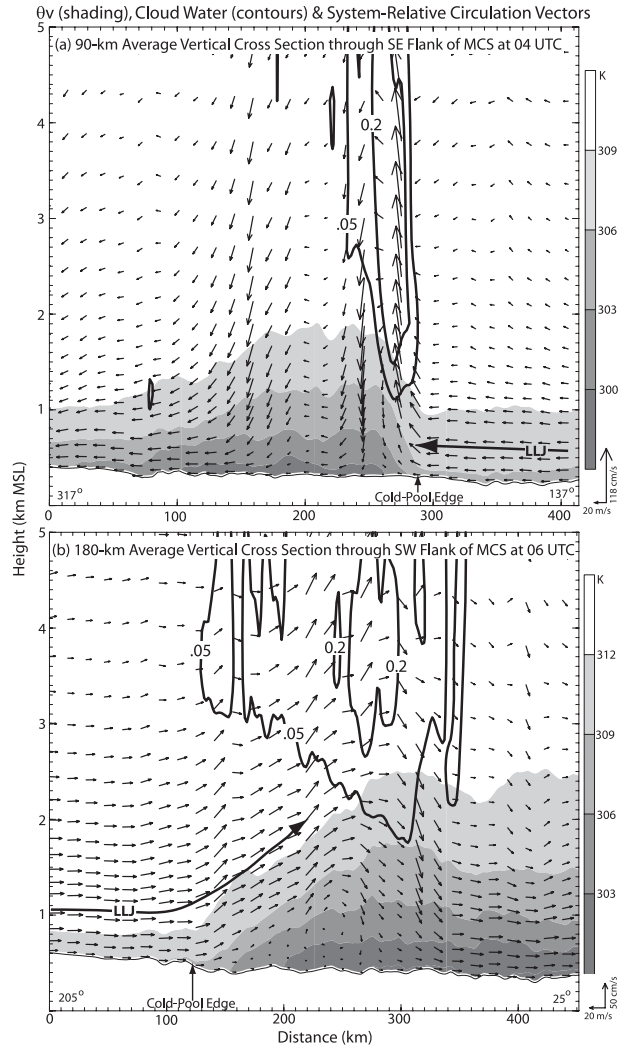


FIG. 18. Vertical cross sections of virtual potential temperature (shading), cloud water exceeding  $0.05$  and  $0.2 \text{ g kg}^{-1}$  (bold contours), and system-relative circulation vectors with respect to motion of the leading edge of the surface virtual potential temperature gradient. These vertical cross sections are averaged for 90 and 180 km, respectively, across transects displayed in (a) Fig. 17b and (b) Fig. 17d. In each panel the nocturnal LLJ is indicated schematically by the bold line with an arrow.

In the late evening along the southeast flank (Fig. 18a), significant vertical shear of  $12\text{--}14 \text{ m s}^{-1}$  occurring in the layer beginning at the height of the southerly jet and extending through the cold pool depth helps sustain upright deep convection at its leading edge through the horizontal vorticity balance mechanism of Rotunno et al. (1988). This result is consistent with the simulations of Parker (2008), which indicate that convection can remain primarily surface based even after significant nocturnal cooling.

However, as the LLJ strengthens and veers overnight, larger-scale (isentropic) ascent associated with warm advection becomes the dominant organization mechanism on the southwest flank of the MCS. Here the cold pool results from modification of the west–east-oriented surface front (Fig. 12) by convection. In contrast to the earlier situation on the southeast flank (Fig. 18a), only weak sporadic cells are triggered at the much shallower cold-pool edge (Fig. 18b) despite comparable vertical shear. Instead, the most intense convection does not occur until  $\sim 150$  km to the rear, where more gradual approximate isentropic ascent above the stable air (Fig. 18b) has brought the LLJ air to near saturation (e.g., Trier and Parsons 1993). We also find narrower zones of sharper lifting well behind the cold-pool edge where both LLJ air and stable air beneath the frontal surface can contribute to the most intense convection in vertical cross sections without line averaging (not shown). Schumacher and Johnson (2008) have shown that such localization of the most intense convection can result from gravity waves forced by diabatic heating.

### 7. Water budget for the heavy precipitation region within the latitudinal corridor

The analysis from the previous section has established the importance of the nocturnal LLJ forcing of convection in the simulations. However, the jet originates over dry soils located southwest of the CPL corridor region, which itself has very moist soil (Fig. 19) due in part to repeated heavy rainfall (Fig. 4a). Mean daytime subsidence occurs in the LLJ origination region (Fig. 9d), resulting in dry conditions above the PBL. This condition combined with strong sensible heating (Fig. 12) results in PBL drying associated with vertical mixing prior to the nightly jet intensification. Thus, while the importance of LLJ-related moisture transport on seasonal and continental scales has been well established (e.g., Helfand and Schubert 1995; Higgins et al. 1997), its role relative to that of local evaporation on the diurnal water cycle of the mesoscale rainfall corridor of the current simulations is not immediately obvious.

To investigate further, we calculate a mesoscale water budget over the CPL region (Fig. 20) for days 4–10 of the simulation using

$$\frac{\partial W}{\partial t} = E - P - \frac{1}{g} \int_0^{p_0} \nabla \cdot q_T \mathbf{V} dp, \quad (2)$$

where  $W$  is the vertically integrated total water substance  $q_T$  (including water vapor  $q_v$  and all species of hydrometeors),  $E$  is the surface evaporation (from both the ground and vegetation canopy),  $P$  is surface precipitation, and  $\mathbf{V}$  is the horizontal vector velocity. The terms in

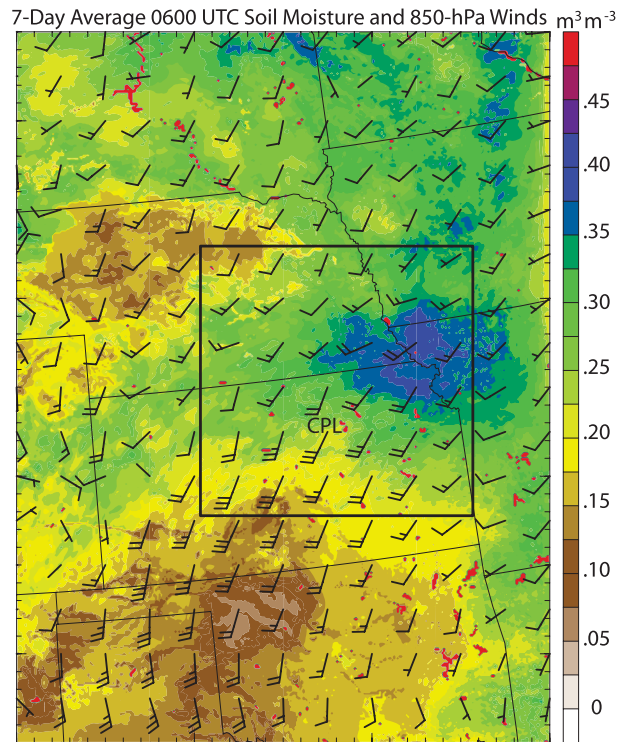


FIG. 19. Seven-day average of 0600 UTC top 0.1-m volumetric soil moisture and 850-hPa wind for days 4–10 of the control simulation. The rectangle encloses the  $450 \times 450$  km<sup>2</sup> CPL region over which the moisture budget in Fig. 20 is calculated.

Eq. (2) are computed at each horizontal grid point and are then horizontally averaged over the  $450 \text{ km} \times 450 \text{ km}$  region.

Figure 20a indicates important contributions to the total column water from both evaporation and vertically integrated moisture flux convergence [term 3 on the right side of (2)]. Here, there is a positive midday  $W$  tendency due to evaporation, a positive evening  $W$  tendency due to moisture flux convergence, and a negative  $W$  tendency overnight due to removal of column water by precipitation. Averaged over the entire diurnal cycle, evaporation contributes  $4.8 \text{ mm day}^{-1}$  and moisture flux convergence contributes  $4.0 \text{ mm day}^{-1}$ , while precipitation removes  $9.6 \text{ mm day}^{-1}$ . The large cancellation between the evening moisture flux convergence and daytime moisture flux divergence (Fig. 20a) has also been documented in regional-scale moisture budgets (e.g., Berbery and Rasmusson 1999).

The large increase in vertically integrated moisture flux convergence prior to heavy nighttime precipitation within the corridor (Fig. 20a), together with the fact much of it can be accounted for by considering only what happens in the 950–700-hPa layer (Fig. 20b), is indicative of the LLJ's importance for moisture transport

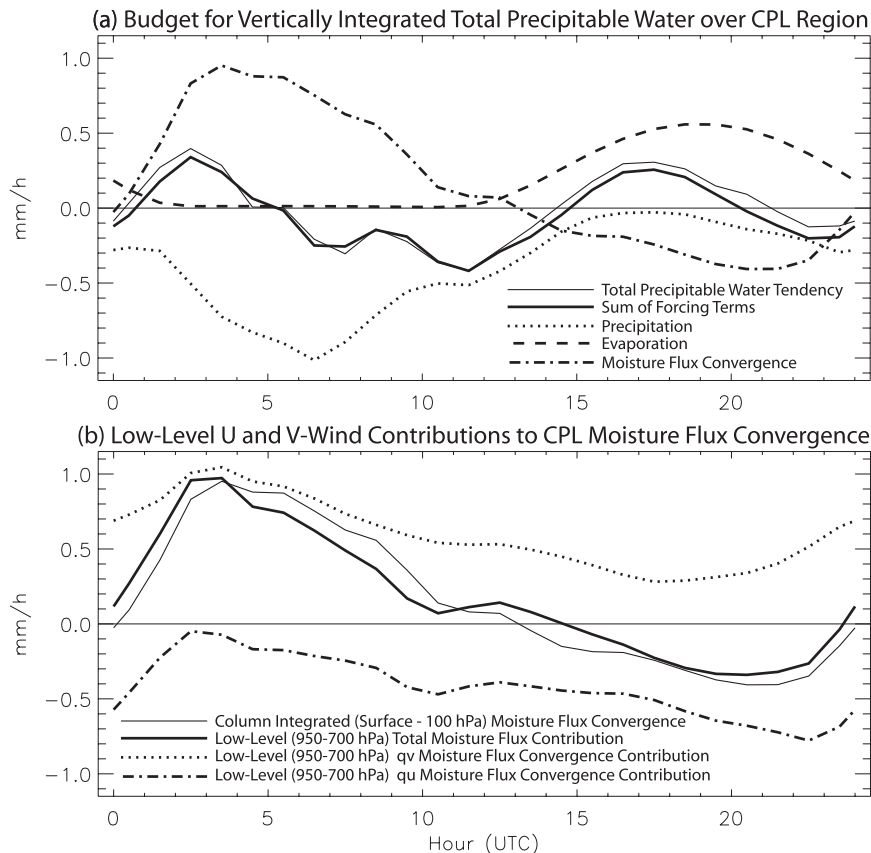


FIG. 20. Seven-day-averaged diurnal cycle of (a) the budget for vertically integrated total precipitable water (water vapor, cloud, and precipitation hydrometeors) over the heavy rainfall CPL region of Fig. 19 (cf. Fig. 4a), and (b) the lower-tropospheric contribution of the vertically integrated moisture flux convergence part of the total budget.

into the mesoscale region. Further understanding of factors influencing the moisture transport throughout the diurnal cycle may be gained by applying the divergence theorem,

$$\begin{aligned}
 & -\frac{1}{g} \int_{p=700\text{hPa}}^{p=950\text{hPa}} \iint (\nabla \cdot q_T \mathbf{V}) dx dy dp \\
 & = -\frac{1}{g} \int_{p=700\text{hPa}}^{p=950\text{hPa}} \oint (q_T \mathbf{V} \cdot d\mathbf{n}) dp, \quad (3)
 \end{aligned}$$

to calculate the components of the total moisture flux,  $q_T u$  and  $q_T v$ , along the perimeter of the CPL region (Fig. 20b) and by examination of Hovmöller diagrams from which we can infer the approximate mean components,  $\bar{q}_v \bar{u}$  and  $\bar{q}_v \bar{v}$ , of these fluxes (Fig. 21).

The afternoon moisture flux divergence results from a net negative zonal flux of moisture (Fig. 20b) and is consistent with divergence of the mean (i.e.,  $y$  averaged) zonal wind in the presence of an eastward-directed horizontal moisture gradient (Fig. 21a). Here the di-

vergence is associated with the flow near the western edge of the CPL region ( $\sim 100^\circ\text{W}$ ) being accelerated weakly westward toward the mountains during the afternoon as part of the MPS circulation (Fig. 9c). The moisture flux convergence into the CPL region at night is associated with both an increase in the net positive meridional flux of moisture and a decrease in the magnitude of the negative zonal flux (Fig. 20b). During the onset of the southerly LLJ, the net positive meridional moisture flux occurs despite slightly lower mean (i.e.,  $x$  averaged) moisture values to the south (Fig. 21b). This indicates that the mesoscale convergence (Fig. 21b), rather than horizontal moisture advection, is responsible for the moisture convergence and increase in precipitable water during the evening from 0100 to 0500 UTC (Fig. 20a). In this way the role of the LLJ in mid-to-late summer multiday west-east-oriented corridors of heavy precipitation over the CPL may differ from that in other situations, where in addition to convergence the LLJ is commonly associated with strong horizontal moisture advection.

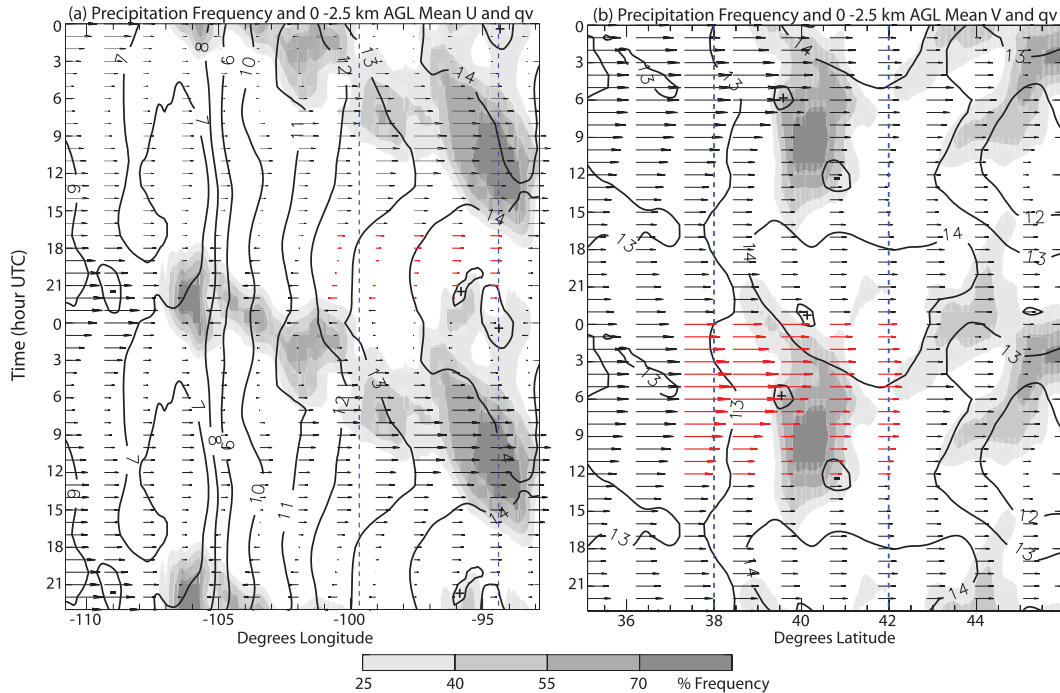


FIG. 21. Seven-day-averaged (days 4–10) Hovmöller diagrams of mean (a)  $y$ -averaged ( $38^{\circ}$ – $42^{\circ}$ N)  $u$ -component wind and water vapor mixing ratio ( $\text{g kg}^{-1}$ ) through 0–2.5 km AGL, and (b)  $x$ -averaged ( $99.8^{\circ}$ – $94.4^{\circ}$ W)  $y$ -component wind and water vapor mixing ratio ( $\text{g kg}^{-1}$ ) through 0–2.5 km AGL. The shaded field is smoothed diurnal precipitation frequency exceeding  $0.25 \text{ mm h}^{-1}$  averaged over the abovementioned regions. The dashed vertical lines in each panel represent the boundaries of the CPL region (Fig. 19) over which the moisture budget in Fig. 20 was calculated. The red vectors highlight times and locations discussed in the text.

## 8. Summary and discussion

This study examines the role of terrain-induced wind systems on the diurnal cycle of summertime precipitation that develops in the lee of the Rocky Mountains and the adjacent plains of the central United States. The precipitation life cycle is simulated using a three-dimensional version of the WRF model with explicit deep convection. The model is initialized using monthly averaged conditions from July 2001 and is integrated for 10 days. The large-scale pattern resulting from the monthly averaged condition (Fig. 3) represents a common midsummer situation characterized by a lack of deep baroclinity and relatively weak background flow conditions. This pattern is often associated with active midsummer convective periods over the Rockies and central United States, which display a particularly high degree of repetitive behavior in successive diurnal cycles.

During the 10-day model integration the temporal variations along the lateral boundaries of the model are constrained to be the same each day. The averaging inherent in this experimental design mitigates the effects of upstream transient disturbances and thus allows a direct assessment of the impact of diurnally varying flow

systems, including the MPS and the nocturnal LLJ, on the domainwide diurnal cycle of precipitation and the water budget within the CPL region where the heaviest rain occurs.

Despite the relative simplicity of the model initial and lateral boundary conditions, many observed features of the July 2001 precipitation climatology and the more general diurnal cycle of continental warm-season precipitation are reproduced. These include an afternoon maximum of precipitation frequency in the mountains followed by a narrow west–east-oriented corridor of enhanced precipitation frequencies from late evening through sunrise on the plains. The nocturnal corridor of convection organizes within a quasi-stationary surface frontal zone, whose location and intensity is itself influenced by the repeated convection episodes. Although upstream transient weather disturbances may enhance and influence longevity of some midsummer precipitation episodes, the current findings suggest they are not essential to the basic development and diurnal cycles of these episodes.

During the afternoon the CPL region east of the mountains is situated within the weakly subsiding branch of the MPS. This region therefore has limited

afternoon convection despite maximum daily thermodynamic energy being approximately in phase with net solar heating. Within the nocturnal precipitation corridor afternoon convection is further inhibited by reduced daytime sensible heat flux and possibly by additional contributions to lower- to midtropospheric subsidence occurring in the wake of the decayed antecedent nocturnal convection. Together these factors may augment the larger-scale MPS in contributing to slower PBL growth and removal of the inversion above.

Farther west, the ascending branch of the afternoon MPS is maximized over the mountains. However, its associated mountain convection does not progress eastward. Instead, it is the afternoon convection focused along west–east-oriented ridges of much lower altitude in the immediate lee of the mountains that contributes to the embryonic stages of subsequent eastward-progressing nocturnal convection on the high plains (102°–98°W). The nocturnal LLJ significantly enhances the lower tropospheric vertical shear and warm advection near the west–east-oriented surface frontal zone at night, both of which favor upscale growth of convection. This is consistent with the shift in maximum precipitation frequencies to the west–east corridor on the plains overnight.

The diurnal veering of the LLJ results in a westward shift of conditions most favorable for convection toward sunrise. This promotes local generation of convection as opposed to continuous eastward progression of preexisting convection. This aspect of the nocturnal convection on the plains is also evident in observationally based climatologies of warm-season heavy rainfall corridors (e.g., Tuttle and Davis 2006).

The degree to which locally initiating nocturnal convection dominates long-lived progressive convection originating well upstream likely depends on large-scale environmental conditions (e.g., CAPE, mean flow, and vertical shear) and whether progressive mesoscale disturbances (e.g., midlevel short waves, mesoscale convective vortices) exist to help organize convection. For instance, the simulated long-lived, rapidly translating rain streaks emphasized by Trier et al. (2006) consisted of MCSs similar to the progressive derechos that occurred in similar environments of strong midlevel westerlies and large CAPE reported by Johns and Hirt (1987). There, in addition to supporting rapidly translating MCSs, the stronger midlevel westerlies alter the vertical shear profile such that a large component of westerly shear remains overnight even in the presence of the nocturnal LLJ. The westerly shear favors continuous redevelopment on the forward (eastern) flank of the MCSs, where strong cold pools favored by large environmental CAPE promote propagation that actually

adds to the eastward progression. This contrasts with the MCS back-building scenario in the current simulations where shorter-lived eastward translating rain streaks develop successively westward late at night in an environment that features lesser CAPE and weaker midlevel westerlies.

The repetitive nature of heavy precipitation within the CPL corridor on successive nights contributes to large soil moisture values. However, effects of daytime evaporation on the water cycle in the precipitation corridor are strongly opposed by the vertically integrated moisture divergence associated with the subsiding branch of the MPS. The nocturnal LLJ is therefore crucial to the net import of moisture into the heavy precipitation region. Since the LLJ originates within a dry afternoon PBL underneath a persistent midtropospheric anticyclone, the net import of water vapor responsible for evening increases in precipitable water over the rainfall corridor results from horizontal convergence instead of horizontal moisture advection.

*Acknowledgments.* This research has been supported by The Institute for Integrative and Multidisciplinary Earth Studies (TIIMES) Water Cycle Program at the National Center for Atmospheric Research. The authors thank John Tuttle (NCAR) for his help in producing Fig. 1. John Tuttle and Rit Carbone (NCAR) are acknowledged for their comments on the manuscript. Comments from William Cotton (Colorado State University) and an anonymous reviewer also resulted in clarifications. Any opinions, findings, conclusions, or recommendations expressed in this publication are those of the authors and do not necessarily reflect the views of the National Science Foundation.

#### REFERENCES

- Augustine, J. A., and F. Caracena, 1994: Lower-tropospheric precursors to nocturnal MCS development over the central United States. *Wea. Forecasting*, **9**, 116–135.
- Barnes, S. L., F. Caracena, and A. Marroquin, 1996: Extracting synoptic-scale diagnostic information from mesoscale models: The Eta Model, gravity waves, and quasi-geostrophic diagnostics. *Bull. Amer. Meteor. Soc.*, **77**, 519–528.
- Berberly, E. H., and E. M. Rasmusson, 1999: Mississippi moisture budgets on regional scales. *Mon. Wea. Rev.*, **127**, 2654–2673.
- Bernardet, L., and W. R. Cotton, 1998: Multiscale evolution of a derecho-producing mesoscale convective system. *Mon. Wea. Rev.*, **126**, 2991–3015.
- Blackadar, A. K., 1957: Boundary layer wind maxima and their significance for the growth of nocturnal inversions. *Bull. Amer. Meteor. Soc.*, **38**, 283–290.
- Bryan, G. H., J. C. Wyngaard, and J. M. Fritsch, 2003: Resolution requirements for the simulation of deep moist convection. *Mon. Wea. Rev.*, **131**, 2394–2416.

- Carbone, R. E., and J. D. Tuttle, 2008: Rainfall occurrence in the U.S. warm season: The diurnal cycle. *J. Climate*, **21**, 4132–4146.
- , J. W. Conway, N. A. Crook, and M. W. Moncrieff, 1990: The generation and propagation of a nocturnal squall line. Part I: Observations and implications for mesoscale predictability. *Mon. Wea. Rev.*, **118**, 26–49.
- , J. D. Tuttle, D. A. Ahijevych, and S. B. Trier, 2002: Inferences of predictability associated with warm season precipitation episodes. *J. Atmos. Sci.*, **59**, 2033–2056.
- Chappell, C. F., 1986: Quasi-stationary convective events. *Mesoscale Meteorology and Forecasting*, P. Ray, Ed., Amer. Meteor. Soc., 289–310.
- Chen, F., and J. Dudhia, 2001: Coupling an advanced land surface–hydrology model with the Penn State-NCAR MM5 modeling system. Part I: Model implementation and sensitivity. *Mon. Wea. Rev.*, **129**, 569–585.
- Corfidi, S. F., J. H. Meritt, and J. M. Fritsch, 1996: Predicting the movement of mesoscale convective complexes. *Wea. Forecasting*, **11**, 41–46.
- Cotton, W. R., R. L. George, P. J. Wetzell, and R. L. McAnelly, 1983: A long-lived mesoscale convective complex. Part I: The mountain-generated component. *Mon. Wea. Rev.*, **111**, 1893–1918.
- Dai, A., F. Giorgi, and K. E. Trenberth, 1999: Observed and model-simulated diurnal cycles of precipitation over the contiguous United States. *J. Geophys. Res.*, **104**, 6377–6402.
- Davis, C. A., K. W. Manning, R. E. Carbone, S. B. Trier, and J. D. Tuttle, 2003: Coherence of warm-season continental rainfall in numerical weather prediction models. *Mon. Wea. Rev.*, **131**, 2667–2679.
- Dudhia, J., 1989: Numerical study of convection observed during the Winter Monsoon Experiment using a mesoscale two-dimensional model. *J. Atmos. Sci.*, **46**, 3077–3107.
- Ek, M. B., K. E. Mitchell, Y. Lin, E. Rogers, P. Grummann, V. Koren, G. Gayno, and J. D. Tarpley, 2003: Implementation of Noah land surface model advances in the National Centers for Environmental Prediction operational mesoscale Eta model. *J. Geophys. Res.*, **108**, 8851, doi:10.1029/2002JD003296.
- Fritsch, J. M., R. J. Kane, and C. R. Chelius, 1986: The contribution of mesoscale convective weather systems to the warm-season precipitation in the United States. *J. Climate Appl. Meteor.*, **25**, 1333–1345.
- Hane, C. E., J. A. Haynes, D. L. Andra Jr., and F. H. Carr, 2008: The evolution of morning convective systems over the U.S. Great Plains during the warm season. Part II: A climatology and the influence of environmental factors. *Mon. Wea. Rev.*, **136**, 929–944.
- Helfand, H. M., and S. D. Schubert, 1995: Climatology of the simulated Great Plains low-level jet and its contribution to the continental moisture budget of the United States. *J. Climate*, **8**, 784–806.
- Higgins, R. W., Y. Yao, E. S. Yarosh, J. E. Janowiak, and K. C. Mo, 1997: Influence of the Great Plains low-level jet on summertime precipitation and moisture transport over the central United States. *J. Climate*, **10**, 481–507.
- Holton, J. R., 1967: The diurnal boundary layer wind oscillation above sloping terrain. *Tellus*, **19**, 199–205.
- Hong, S.-Y., J. Dudhia, and S.-H. Chen, 2004: A revised approach to ice microphysical processes for the bulk parameterization of clouds and precipitation. *Mon. Wea. Rev.*, **132**, 103–120.
- Janjić, Z. I., 1990: The step-mountain coordinate: Physical package. *Mon. Wea. Rev.*, **118**, 1429–1443.
- , 1994: The step-mountain eta coordinate model: Further developments of the convection, viscous sublayer, and turbulence closure schemes. *Mon. Wea. Rev.*, **122**, 927–945.
- Jiang, X., N.-C. Lau, I. M. Held, and J. J. Ploshay, 2007: Mechanisms of the Great Plains low-level jet as simulated in an AGCM. *J. Atmos. Sci.*, **64**, 532–547.
- Jirak, I. L., and W. R. Cotton, 2007: Observational analysis of the predictability of mesoscale convective systems. *Wea. Forecasting*, **22**, 813–838.
- Johns, R. H., and W. D. Hirt, 1987: Derechos: Widespread convectively induced windstorms. *Wea. Forecasting*, **2**, 32–49.
- Klemp, J. B., J. Dudhia, and A. D. Hassiotis, 2008: An upper gravity-wave absorbing layer for NWP applications. *Mon. Wea. Rev.*, **136**, 3987–4004.
- Koch, S. E., F. Zhang, M. L. Kaplan, Y.-L. Lin, R. Weglarz, and C. M. Trexler, 2001: Numerical simulations of a gravity wave event over CCOPE. Part III: The role of a mountain–plains solenoid in the generation of the second wave episode. *Mon. Wea. Rev.*, **129**, 909–933.
- Laing, A. G., R. E. Carbone, V. Levizzani, and J. D. Tuttle, 2008: The propagation and diurnal cycles of convection in northern tropical Africa. *Quart. J. Roy. Meteor. Soc.*, **134A**, 93–109.
- Lee, M.-I., and Coauthors, 2007: Sensitivity of horizontal resolution in the AGCM simulations of warm season diurnal cycle of precipitation over the United States and northern Mexico. *J. Climate*, **20**, 1862–1881.
- Maddox, R. A., 1983: Large-scale meteorological conditions associated with mesoscale convective complexes. *Mon. Wea. Rev.*, **111**, 1475–1493.
- McAnelly, R. L., and W. R. Cotton, 1989: The precipitation life-cycle of mesoscale convective complexes over the central United States. *Mon. Wea. Rev.*, **117**, 784–808.
- Mesinger, F., and Coauthors, 2006: North American Regional Reanalysis. *Bull. Amer. Meteor. Soc.*, **87**, 343–360.
- Mlawer, E. J., S. J. Taubman, P. D. Brown, M. J. Iacono, and S. A. Clough, 1997: Radiative transfer for inhomogeneous atmospheres: RRTM, a validated correlated-*k* model for the longwave. *J. Geophys. Res.*, **102** (D14), 16 663–16 682.
- Moncrieff, M. W., and C. Liu, 2006: Representing convective organization in prediction models by a hybrid strategy. *J. Atmos. Sci.*, **63**, 3404–3420.
- Olsson, P. Q., and W. R. Cotton, 1997: Balanced and unbalanced circulations in a primitive equation simulation of a midlatitude MCC. Part II: Analysis of balance. *J. Atmos. Sci.*, **54**, 479–497.
- Parker, M. D., 2008: Response of simulated squall lines to low-level cooling. *J. Atmos. Sci.*, **65**, 1323–1341.
- Raymond, D. J., and H. Jiang, 1990: A theory for long-lived mesoscale convective systems. *J. Atmos. Sci.*, **47**, 3067–3077.
- Rotunno, R., J. B. Klemp, and M. L. Weisman, 1988: A theory for strong, long-lived squall lines. *J. Atmos. Sci.*, **45**, 463–485.
- Schumacher, R. S., and R. H. Johnson, 2008: Mesoscale processes contributing to extreme rainfall in a midlatitude warm-season flash flood. *Mon. Wea. Rev.*, **136**, 3964–3986.
- Skamarock, W. C., and M. L. Weisman, 2009: The impact of positive-definite moisture transport on NWP precipitation forecasts. *Mon. Wea. Rev.*, **137**, 488–494.
- , J. B. Klemp, J. Dudhia, D. O. Gill, D. M. Barker, W. Wang, and J. G. Powers, 2005: A description of the Advanced Research WRF version 2. NCAR Tech. Note TN-468+STR, 88 pp. [Available from NCAR, P.O. Box 3000, Boulder, CO 80307.]
- Toth, J. J., and R. H. Johnson, 1985: Summer surface flow characteristics over northeast Colorado. *Mon. Wea. Rev.*, **113**, 1458–1469.

- Trenberth, K. E., 1999: Atmospheric moisture recycling: Role of advection and local evaporation. *J. Climate*, **12**, 1368–1381.
- Trier, S. B., and D. B. Parsons, 1993: Evolution of environmental conditions preceding the development of a nocturnal mesoscale convective complex. *Mon. Wea. Rev.*, **121**, 1078–1098.
- , and C. A. Davis, 2002: Influence of balanced motions on heavy precipitation within a long-lived convectively generated vortex. *Mon. Wea. Rev.*, **130**, 877–899.
- , —, D. A. Ahijevych, M. L. Weisman, and G. H. Bryan, 2006: Mechanisms supporting long-lived episodes of propagating nocturnal convection within a 7-day WRF model simulation. *J. Atmos. Sci.*, **63**, 2437–2461.
- Tripoli, G. J., and W. R. Cotton, 1989a: Numerical study of an observed orogenic mesoscale convective system. Part I: Simulated genesis and comparison with observations. *Mon. Wea. Rev.*, **117**, 273–304.
- , and —, 1989b: Numerical study of an observed orogenic mesoscale convective system. Part II: Analysis of governing dynamics. *Mon. Wea. Rev.*, **117**, 305–328.
- Tucker, D. F., and N. A. Crook, 2005: Flow over heated terrain. Part II: Generation of convective precipitation. *Mon. Wea. Rev.*, **133**, 2565–2582.
- Tuttle, J. D., and C. A. Davis, 2006: Corridors of warm season precipitation in the central United States. *Mon. Wea. Rev.*, **134**, 2297–2317.
- Wallace, J. M., 1975: Diurnal variations in precipitation and thunderstorm frequency over the conterminous United States. *Mon. Wea. Rev.*, **103**, 406–419.
- Wang, C.-C., G. T.-J. Chen, and R. E. Carbone, 2004: A climatology of warm-season cloud patterns over East Asia based on GMS infrared brightness temperature observations. *Mon. Wea. Rev.*, **132**, 1606–1629.
- Wetzel, P. J., W. R. Cotton, and R. L. McAnelly, 1983: A long-lived mesoscale convective complex. Part II: Evolution and structure of the mature complex. *Mon. Wea. Rev.*, **111**, 1919–1937.
- Zhang, D.-L., W.-Z. Zheng, and Y.-K. Xue, 2003: A numerical study of early summer regional climate and weather over LSA-East. Part I: Model implementation and verification. *Mon. Wea. Rev.*, **131**, 1895–1909.